ALMA MATER STUDIORUM
UNIVERSITÀ DI BOLOGNA

DOTTORATO DI RICERCA IN

BIOLOGIA CELLULARE E MOLECOLARE

Ciclo 38

Settore Concorsuale: 05/I1 - GENETICA

Settore Scientifico Disciplinare: BIO/18 – GENETICA

ATRX SAFEGUARDS GENOME ARCHITECTURE AND PREVENTS LTR-DRIVEN GENE ACTIVATION

Presentata da: Kelvin Maduabuchi Okpokpo

Coordinatore Dottorato

Anna Maria Porcelli

Supervisore

Giovanni Perini

Co-supervisore

Kavitha Sarma

Esame Finale anno 2026

atrx safeguards genome architecture and prevents ltr-driven gene activation

ATRX is a chromatin remodeler with diverse functions in histone H3.3 deposition, silencing of repetitive elements, and genome stability (Hoelper et al., 2017; Voon and Wong, 2016). ATRX regulates DNA methylation and binding of the architectural protein CTCF at imprinted genes (Gibbons et al., 2000; Kernohan et al., 2010), but whether it has a larger role in genome organization is unclear. Here, we use an ATRX knockout model to probe the effects of ATRX loss on genome-wide CTCF localization and 3D chromatin structure. We find that ATRX loss results in widespread changes in both CTCF and DNA methylation associated with dysregulation of H3.3 deposition and relocalization of the HIRA complex. Furthermore, we observe profound alterations to genome organization at every scale, from blurring of A/B compartments to restructuring of TADs and chromatin loops. While some of these changes are associated with CTCF dysregulation, others are linked to weakening of replication timing and derepression of long terminal repeat retrotransposons. Our findings establish ATRX as a regulator of genome organization in development and disease.

References

- Gibbons, R.J., McDowell, T.L., Raman, S., O'Rourke, D.M., Garrick, D., Ayyub, H., Higgs, D.R., 2000. Mutations in ATRX, encoding a SWI/SNF-like protein, cause diverse changes in the pattern of DNA methylation. Nat. Genet. 24, 368–371. https://doi.org/10.1038/74191
- Hoelper, D., Huang, H., Jain, A.Y., Patel, D.J., Lewis, P.W., 2017. Structural and mechanistic insights into ATRX-dependent and -independent functions of the histone chaperone DAXX. Nat. Commun. 8, 1193. https://doi.org/10.1038/s41467-017-01206-y
- Kernohan, K.D., Jiang, Y., Tremblay, D.C., Bonvissuto, A.C., Eubanks, J.H., Mann, M.R.W., Bérubé, N.G., 2010. ATRX Partners with Cohesin and MeCP2 and Contributes to Developmental Silencing of Imprinted Genes in the Brain. Dev. Cell 18, 191–202. https://doi.org/10.1016/j.devcel.2009.12.017
- Voon, H.P.J., Wong, L.H., 2016. New players in heterochromatin silencing: histone variant H3.3 and the ATRX/DAXX chaperone. Nucleic Acids Res. 44, 1496–1501. https://doi.org/10.1093/nar/gkw012

ATRX safeguards genome architecture and prevents LTR-driven gene activation

INTRODUCTION

Chromatin Regulator Mutations in Neurodevelopment Disorders

Neurodevelopmental disorders (NDDs) encompass a diverse group of conditions arising from early disruptions in brain development, beginning as early as conception and extending through childhood. These disruptions result in a broad and heterogeneous spectrum of clinical outcomes, including intellectual disability (ID), autism spectrum disorder (ASD), attention-deficit/hyperactivity disorder (ADHD), schizophrenia (SCZ), and mood disorders such as bipolar disorder (BD) and major depressive disorder (MDD) (Ernst, 2016). NDDs are typically diagnosed during early childhood and can be attributed to both genetic and non-genetic factors (Mossink et al., 2021). Among the genetic contributors, mutations in chromatin remodeling genes have emerged as significantly enriched in large cohorts of NDD patients (Ciptasari and van Bokhoven, 2020; Pinto et al., 2014; The DDD Study et al., 2014).

Chromatin remodelers are specialized proteins that modify chromatin structure through distinct mechanisms, including nucleosome sliding (movement of histone octamers along DNA), alteration of nucleosomal DNA conformation, and histone variant exchange (replacement of canonical histones with variants such as H3.3) (Tyagi et al., 2016). These remodeling activities enable context-dependent gene expression, tailored to specific cell types and developmental demands, underscoring their critical role in neurodevelopmental regulation. Based on their molecular mode of action, chromatin remodelers are broadly classified into two categories: those that mediate posttranslational modifications of histones, and those that alter histone-DNA contacts within nucleosomes via ATP hydrolysis (Tyagi et al., 2016). Several NDDs have been directly linked to mutations in chromatin remodeling genes. For instance, SETDB1

encodes a histone methyltransferase that catalyzes H3K9 trimethylation, promoting transcriptional silencing of repetitive elements and genes; its disruption has been associated with ASD (Cukier et al., 2012); CHD8 one of the most frequently mutated genes in autism, function as an ATP-dependent helicase that anti regulates Wnt- catenin signaling (Neale et al., 2012; Xu et al., 2018); KMT2A (MLL1) is a histone H3K4 methyltransferase essential for transcriptional activation during embryonic development; mutations in this gene cause Wiedemann–Steiner syndrome, characterized by intellectual disability and dysmorphic features (Jones et al., 2012); HDAC2, a class I histone deacetylase, removes acetyl groups from histones to repress gene expression; its dysregulation has been implicated in Cornelia de Lange syndrome, affecting cognitive and behavioral function (Wagner et al., 2019); Lastly, ARID2, a component of the SWI/SNF complex, facilitates chromatin remodeling via ATP hydrolysis and is associated with Coffin–Siris syndrome, which presents with developmental delay and craniofacial anomalies (Bramswig et al., 2017).

ATRX Dysfunction in Human Disease: From ATR-X Syndrome to Cancer

In the early 1990s, Gibbons et al. analyzed clinical and genetic data from several families, identifying an inheritance pattern linked to the X chromosome. This observation suggested the existence of a novel genetic syndrome, distinct from other forms of cognitive impairment. Based on the recurrent traits observed in affected individuals (alpha-thalassemia, intellectual disability, and X-linked transmission) the acronym **ATRX** was coined (Gibbons et al., 1991).

Four years later, the same research group identified the locus of the gene responsible for the syndrome to the long arm of the X chromosome (Xq13.3). The gene encodes a protein of approximately 280 kDa, characterized by regions resembling those found in transcriptional regulators and proteins involved in chromatin remodeling (Gibbons et al., 1995).

This discovery established the first direct link between ATRX dysfunction and a human disorder with both neurological and hematological manifestations. The majority of ATR-X

syndrome–associated mutations are missense mutations (that result in loss of function) cluster within two key domains of the ATRX protein: the ADD domain (~50%) and the SNF2-like/helicase domain (~30%) (Argentaro et al., 2007; Gibbons et al., 2008). Mutations in the ADD domain, which mediates histone recognition and chromatin targeting, are typically associated with more severe psychomotor impairment than those affecting the helicase domain, which governs ATP-dependent nucleosome remodeling (Badens et al., 2006). Due to X-chromosome inactivation skewing, female carriers are usually asymptomatic, while male patients, lacking a second compensatory allele, exhibit the full clinical spectrum of the disorder (Wada et al., 2005).

Beyond its role in syndromic neurodevelopment, ATRX has emerged as a key player in cancer biology. Studies have shown that individuals with ATR-X syndrome may carry a genetic predisposition to osteosarcoma, suggesting that ATRX dysfunction may contribute to tumorigenesis (Ji et al., 2017). More broadly, ATRX mutations are frequently observed in a range of cancer, including low-grade gliomas, pediatric glioblastoma multiforme, adrenocortical carcinoma, osteosarcoma, and neuroblastoma (Dyer et al., 2017). According to data from cBioPortal (accessed September 27, 2025), ATRX alterations are most prevalent in brain gliomas and sarcomas.

Unlike the domain specific mutations seen in ATR-X syndrome, tumor associated ATRX mutations are distributed throughout the gene and often result in non-functional or loss of the protein due to missense point mutations, frameshifts, or nonsense variants (Dyer et al., 2017; Iwase et al., 2011).

One of ATRX's most critical roles in cancer cells is its involvement in telomere regulation. Loss of ATRX is a hallmark of over 90% of cancer cell lines that utilize the alternative lengthening of telomeres (ALT) mechanism for immortalization (Lovejoy et al., 2012). This strongly supports the hypothesis that ATRX acts as a suppressor of the ALT pathway, maintaining telomere integrity and preventing aberrant recombination. Moreover, ATRX mutations are often mutually exclusive with TERT promoter mutations, which reactivate telomerase expression. This mutual exclusivity suggests that tumors adopt distinct strategies for telomere maintenance, either through TERT activation or

ALT pathway engagement, both of which confer a selective advantage during tumor progression (Killela et al., 2013).

These findings position ATRX not only as a critical regulator of neurodevelopment but also as a tumor suppressor whose disruption contributes to oncogenic transformation.

Molecular Domains of ATRX: Structural Overview

Following the identification of **ATRX** as the causative gene of ATR-X syndrome, numerous studies have characterized its structure and functional interactions, revealing its central role in maintaining genomic stability particularly through its involvement in chromatin remodeling and telomere maintenance.

ATRX is a highly conserved protein between mouse and human, sharing 85% sequence homology. Homologous proteins have also been identified in *Drosophila melanogaster* (dATRX; 66% homology) and *Caenorhabditis elegans* (XNP-1; 52% homology)(Lee et al., 2007; Valenzuela et al., 2021).

The ATRX protein exhibits a modular organization with highly conserved domains (Fig. 1). At the N-terminal, it contains the ADD domain (ATRX–DNMT3–DNMT3L), named for its cysteine-rich motifs that resemble those found in DNMT3 proteins involved in DNA methylation (Argentaro et al., 2007). This domain includes a GATA-like zinc finger and a PHD-like zinc finger, which are essential for recognizing unmethylated lysine 4 (H3K4) and di- or trimethylated lysine 9 (K9me2/3) on histone H3 (Dhayalan et al., 2011; Eustermann et al., 2011b; Iwase et al., 2011). At the C-terminal, ATRX contains an ATPase/helicase domain, which is shared with members of the SWI/SNF family but absent in the truncated isoform of approximately 200 kDa (Garrick et al., 2004).

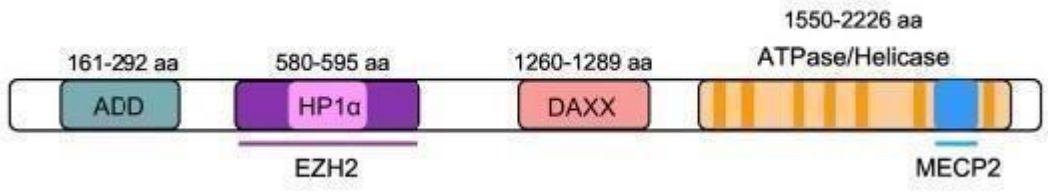

Fig.1 The different domains of the ATRX protein (Aguilera and López-Contreras, 2023).

Role of ATRX in H3. 3 Deposition

The deposition of the histone variant H3.3 is a fundamental process for preserving chromatin integrity and modulating gene expression across both transcriptionally active and repressive genomic regions. H3.3 is enriched at sites of dynamic chromatin remodeling, including promoters, enhancers, telomeres, and heterochromatic domains, where it contributes to nucleosome stability and epigenetic memory (Choi et al., 2024).

Unlike canonical histones H3.1 and H3.2, which are incorporated during DNA replication via the CAF-1 chaperone, H3.3 is deposited independently of replication, allowing for histone replacement and chromatin remodeling even in non-dividing cells. This replication-independent pathway enables continuous histone turnover and transcription coupled nucleosome assembly, mediated by specialized chaperones such as HIRA and ATRX/DAXX, which operate in distinct genomic contexts (Lewis et al., 2010; Ray-Gallet et al., 2011; Tagami et al., 2004).

The ATRX–DAXX complex functions as a dedicated chaperone for H3.3, directing its deposition to repetitive regions of the genome, including telomeres, pericentromeres, and retrotransposons. This targeted incorporation of H3.3 promotes the formation of compact heterochromatin, reinforcing transcriptional silencing and protecting genome stability (Hoelper et al., 2017; Voon and Wong, 2016).

For instance, ATRX plays a central role in silencing transposable elements such as IAPs and ETn/MusD, where H3.3 deposition precedes the recruitment of SETDB1 and TRIM28/KAP1, which catalyze H3K9 trimethylation. Loss of H3.3 at these sites leads to a reduction in H3K9me3, derepression of retrotransposons, and aberrant activation of nearby genes, underscoring the importance of ATRX mediated histone deposition in safeguarding transcriptional fidelity (Elsässer et al., 2015b).

A similar mechanism operates at imprinted loci in murine embryonic stem cells, where ATRX deficiency impairs H3.3 incorporation, resulting in loss of H3K9me3, transcriptional derepression, and disruption of allele-specific expression. These findings suggest that ATRX is essential for maintaining the epigenetic memory of silencing, particularly in regions governed by parent of origin imprinting (Voon et al., 2015). ATRX recruitment to heterochromatin is mediated by its ADD domain, which recognizes a

unique combination of histone marks: unmethylated lysine 4 (H3K4me0) and trimethylated lysine 9 (H3K9me3) on histone H3. In concert with HP1, which also binds H3K9me3, ATRX forms a tripartite complex that interprets the histone code and directs H3.3 deposition to transcriptionally silent regions. This combinatorial recognition ensures precise targeting of ATRX to heterochromatin and reinforces the structural and functional integrity of these domains (Eustermann et al., 2011b).

In human cells, the PML protein has been identified as a key organizer of large heterochromatic structures known as PML-associated domains (PADs). These domains serve as scaffolds for ATRX/DAXX mediated H3.3 deposition. Disruption of PML alters the epigenetic landscape of PADs, shifting the balance from H3K9me3 to H3K27me3, and impairs the silencing capacity of the ATRX/DAXX complex, highlighting the role of nuclear architecture in chromatin regulation (Delbarre et al., 2017).

Recent evidence also reveals that the ATRX/DAXX/H3.3 complex is active in euchromatic regions, particularly at promoters, enhancers, and CpG islands, where it associates with G-rich sequences. This suggests a broader functional repertoire for ATRX/DAXX, extending beyond heterochromatin to include active regulatory elements, where it may cooperate with the HIRA complex to facilitate transcription coupled H3.3 deposition and maintain chromatin accessibility (Truch et al., 2022).

Role of HIRA in H3.3 Deposition

The HIRA complex is one of the two principal histone chaperones responsible for the replication independent deposition of the histone variant H3.3, functioning in parallel with the ATRX–DAXX complex. HIRA primarily targets euchromatic regions, such as promoters, enhancers, and gene bodies, where it facilitates transcription coupled nucleosome turnover. In contrast, DAXX mediates H3.3 deposition at heterochromatic domains, including telomeres and repetitive elements, often in cooperation with ATRX. This division of labor ensures that H3.3 is distributed spatially and temporally across the genome to support both gene activation and transcriptional silencing, thereby maintaining cellular identity and enabling a robust response to epigenetic stress (Choi et al., 2024).

Recent studies have further explored HIRA's role in embryonic stem cells (ESCs), where it contributes to the establishment of a poised chromatin state at key developmental genes. The HIRA complex, composed of HIRA, UBN1, and CABIN1, not only facilitates H3.3 deposition but also coordinates the incorporation of H2A.Z, another histone variant associated with transcriptional regulation. This dual deposition is mediated in part through interaction with the SRCAP complex, which specializes in H2A.Z loading. Together, these activities prime regulatory regions for transcriptional activation, maintaining genes in a transcriptionally competent but inactive state. This poised configuration is essential for preserving pluripotency and enabling a rapid transcriptional response upon differentiation signals (Yang et al., 2022).

Additional evidence shows that HIRA mediated H3.3 deposition enhances chromatin accessibility and facilitates the recruitment of transcription factors and coactivators at active promoters. Specifically, H3.3 incorporation promotes the enrichment of p300, a histone acetyltransferase, and the accumulation of H3K27ac, a mark associated with active enhancers and promoters. Loss of H3.3 leads to diminished chromatin openness and reduced coactivator binding, impairing the ability of ESCs to activate lineage specific transcriptional programs. This underscores the importance of HIRA in maintaining a chromatin environment conducive to gene expression and developmental plasticity (Tafessu et al., 2023).

Further insights into HIRA's function have emerged from studies in ALT (Alternative Lengthening of Telomeres) cancer cells, where the ATRX/DAXX complex is frequently inactivated. In these contexts, HIRA assumes a compensatory role, depositing H3.3 at telomeres to preserve chromatin structure and prevent genomic instability. This activity is critical for limiting the formation of R-loops, which are RNA–DNA hybrids that arise during transcription and can interfere with replication fork progression. By mitigating transcription–replication conflicts, HIRA safeguards telomere integrity and supports the survival of ALT-positive tumor cells. These findings suggest a functional redistribution between the two chaperone systems, with HIRA partially substituting for ATRX at specific loci to maintain chromatin homeostasis in cancer (Lynskey et al., 2024).

The Role of ATRX in Transposable Element Regulation

In the context of epigenetic regulation, transposable elements (TEs) pose a significant challenge to genome stability due to their inherent mobility and capacity for selfreplication. These elements include LINE-1 retrotransposons, endogenous retroviral elements (ERVs), and tandem repeats such as centromeric satellites and telomeric sequences. Although TEs have contributed to evolutionary innovation and genetic diversity, their derepression can lead to chromosomal rearrangements, transcriptional dysregulation, and innate immune activation, mimicking viral infection and triggering inflammatory responses. This dual nature makes their regulation a critical aspect of maintaining genomic and cellular homeostasis (Garcia-Perez et al., 2016).

ATRX has emerged as a key epigenetic regulator of repetitive elements, acting across multiple sequence classes to preserve genomic integrity. In particular, ATRX safeguards tandem repeats such as minor satellites, especially under conditions of global DNA hypomethylation, by promoting the deposition of H3K9me3, a hallmark of constitutive heterochromatin. This activity helps maintain the repressive chromatin architecture necessary to silence these repetitive regions and prevent their transcriptional activation (He et al., 2015).

Beyond tandem repeats, ATRX plays a direct role in the silencing of retrotransposons, notably Intracisternal A Particles (IAPs). It does so by cooperating with the histone methyltransferase SETDB1, which catalyzes the trimethylation of H3K9 at these loci. ATRX facilitates SETDB1 recruitment and stabilizes the heterochromatic state, thereby reinforcing transcriptional repression and preventing retrotransposon mobilization (Sadic et al., 2015b).

This function is part of a broader silencing framework in which ERVs are repressed through a combination of heterochromatin formation and DNA methylation. While ATRX is not the sole factor involved, it contributes to the stabilization of repressive chromatin at ERV loci, working in concert with other epigenetic regulators to ensure long-term silencing. This layered repression is essential for preventing ERV derived transcriptional noise and maintaining cellular identity (Groh and Schotta, 2017).

In the neuronal context, ATRX maintains the silencing of noncoding transcription at centromeric minor satellite sequences, even in response to neuronal stimuli that typically induce chromatin remodeling. This is achieved through ATRX's ability to recognize a combinatorial histone signature, specifically H3K9me3 coupled with serine 10 phosphorylation (S10ph) on histone H3. This dual recognition allows ATRX to tolerate activity dependent chromatin changes while preserving the epigenetic integrity of repetitive regions (Noh et al., 2015).

In mouse embryonic stem cells, the incorporation of H3.3 into repetitive genomic regions has been shown to be indispensable for the formation of heterochromatin and the transcriptional repression of ERVs, particularly the IAP and ETn/MusD families. H3.3 deposition precedes the establishment of repressive marks such as H3K9me3 and is required to initiate and maintain silencing. Loss of H3.3 disrupts this process, leading to ERV activation and compromised genome stability (Elsässer et al., 2015b).

The protective role of ATRX extends to mesenchymal progenitor cells, where its loss results in the derepression of retrotransposons, accompanied by a reduction in H3K9me3 levels. This epigenetic disruption leads to the aberrant activation of differentiation programs, including adipogenic pathways, and alters the transcriptional landscape of progenitor cells. These findings highlight ATRX's role in safeguarding lineage fidelity and preventing premature or inappropriate differentiation (Fang et al., 2024b)

In microglia, the brain's resident immune cells, ATRX deficiency causes derepression of retroelements, which triggers a viral mimicry response. This immune activation leads to the production of interferon stimulated genes and inflammatory mediators, ultimately impacting neuronal function and behavior. The study demonstrates that chromatin remodeling in glial cells is essential not only for immune regulation but also for maintaining neurocognitive health (Shafiq et al., 2025).

Finally, a link has been established between LINE-1 derepression and transcriptional as well as behavioral dysfunctions in autism spectrum disorder (ASD) models. Elevated LINE-1 activity correlates with altered gene expression profiles and behavioral phenotypes, suggesting that ATRX mediated repression of these elements is critical for

neurodevelopmental stability. These findings underscore the importance of transposable element control in the context of ASD pathophysiology (Spirito et al., 2023).

ATRX interaction Network and Disease Relevance

ATRX contains several conserved domains and motifs that mediate protein–protein interactions (Aguilera and López-Contreras, 2023). One such motif, P/LxVxL (Proline/Leucine–Valine–Leucine–x, where x represents any amino acid), enables ATRX to interact with HP1, thereby facilitating its recruitment to heterochromatin (Eustermann et al., 2011a). This interaction is not only essential for ATRX's localization to constitutive heterochromatin but also plays a pivotal role in the formation of senescence-associated heterochromatin foci (SAHF) following genotoxic stress. In the context of therapyinduced senescence, ATRX–HP1 binding enables the chromatin remodeling necessary to silence pro-proliferative genes and enforce a stable cell cycle arrest. Loss of ATRX or disruption of its interaction with HP1 impairs SAHF assembly, allowing damaged cells to escape senescence, a mechanism that contributes to therapy resistance and tumor progression in cancers such as gliomas and sarcomas (Kovatcheva et al., 2017).

ATRX also binds directly to the histone chaperone DAXX, with a minimal region of approximately 30 amino acids being sufficient for this interaction (Wang et al., 2017). This interaction is not only essential for the deposition of the histone variant H3.3 at repetitive genomic regions but also plays a critical role in the DNA damage response (DDR). In a tumor context, ATRX-DAXX complex plays a pivotal role in facilitating p53 chromatin binding and the activation of DNA damage response (DDR) genes. Specifically, Gulve et al., demonstrated that loss of ATRX or DAXX in glioblastoma cells leads to impaired recruitment of p53 to its target promoters following genotoxic stress, resulting in attenuated transcriptional activation of p53-dependent genes such as CDKN1A (p21) and GADD45A. This defect compromises the p53 tumor suppressor

pathway, allowing cells to bypass senescence and cell cycle arrest, thereby promoting genomic instability and tumor progression. Moreover, ATRX/DAXX-deficient cells exhibited ALT-like features, linking this interaction to telomere maintenance mechanisms in cancers that lack telomerase activity (Gulve et al., 2022).

In addition to interacting with proteins, ATRX also associates with specific long noncoding RNAs (lncRNAs) that contribute to the regulation of chromatin architecture. Among these, ChRO1 plays a pivotal role during muscle cell differentiation. Functionally, ChRO1 acts as a molecular scaffold, recruiting the ATRX/DAXX complex to chromocenters and enabling the deposition of the histone variant H3.3, which is critical for chromatin stability. In the absence of ChRO1, ATRX and DAXX fail to accumulate at these sites, resulting in defective H3.3 incorporation, disruption of chromocenter clustering, and accumulation of satellite RNAs, indicative of impaired transcriptional silencing. These defects compromise the formation of repressive chromatin and destabilize nuclear architecture, highlighting the indispensable role of ChRO1 in orchestrating ATRX/DAXX-dependent chromatin remodeling during healthy differentiation (Park et al., 2018).

Another lncRNA is TERRA (Telomeric Repeat-containing RNA), which is transcribed from telomeric regions. TERRA plays a crucial role in the epigenetic regulation of telomeres and can antagonize ATRX by preventing its binding to telomeres, thereby promoting a more open chromatin configuration. This mechanism is particularly relevant in ALT-positive tumors, where loss of ATRX leads to TERRA accumulation and telomeric instability (Tsai et al., 2022).

Furthermore, the ATRX interaction domain with EZH2, the catalytic subunit of PRC2, enables the formation of a ternary ATRX–Xist–PRC2 complex, facilitating the direct binding of PRC2 to Xist RNA in vivo. This interaction is essential for the recruitment of PRC2 to Polycomb target loci during X-chromosome inactivation. ATRX binds both Xist RNA and EZH2, acting as a molecular bridge that stabilizes PRC2 association with chromatin. In the absence of ATRX, PRC2 fails to efficiently bind Xist RNA, resulting in reduced H3K27me3 deposition and defective silencing of X-linked genes. Genome-wide analyses in ATRX-depleted cells revealed a significant loss of PRC2 occupancy at

multiple Polycomb targets, indicating that ATRX is required not only for RNA-mediated recruitment but also for chromatin retention of PRC2. These findings underscore the critical role of ATRX in guiding PRC2 to its targets and maintaining epigenetic repression, and suggest that disruption of this axis may compromise chromatin silencing programs in both developmental and pathological contexts (Sarma et al., 2014).

ATRX also interacts directly with the histone variant macroH2A1.2 to maintain telomeric chromatin compaction. In its absence, macroH2A1.2 is removed in a less regulated manner during replicative stress, promoting the formation of double-strand breaks (DSBs) and the activation of the ALT pathway. This contributes to telomere elongation through recombination-based mechanisms in ATRX-deficient cells (Kim et al., 2019).

In the brain, the recruitment of ATRX to heterochromatin is primarily mediated by MeCP2, a methylation-sensitive chromatin-binding protein that directly interacts with the helicase domain of ATRX (Marano et al., 2019; Nan et al., 2007). This interaction is critical for the proper organization of pericentric heterochromatin during neural differentiation, where ATRX and MeCP2 co-localize at chromocenters to promote chromatin compaction and transcriptional silencing (Marano et al., 2019). Notably, mutations in MeCP2 associated with inherited intellectual disability disrupt this interaction, leading to ATRX mislocalization, loss of heterochromatin integrity, and aberrant expression of repetitive DNA elements (Nan et al., 2007). Beyond their role in heterochromatin maintenance, ATRX and MeCP2 also form a functional complex with the Cohesin subunits SMC1/3, contributing to the developmental silencing of imprinted genes in the mouse brain (Kernohan et al., 2010a). In MeCP2 deficient neural cells, ATRX fails to accumulate at pericentric regions, resulting in defective chromocenter clustering, reduced H3K9me3 enrichment, and compromised nuclear architecture. These defects impair the epigenetic repression of imprinted loci and contribute to neurodevelopmental dysfunction, underscoring the indispensable role of MeCP2 in guiding ATRX mediated chromatin remodeling and transcriptional silencing during brain development (Kernohan et al., 2010a).

ATRX further interacts with NBS1, supporting the activity of the MRN complex in the repair of double-strand breaks (DSBs), and with FANCD2 within the Fanconi anemia

pathway for the removal of interstrand crosslinks (ICLs). In both cases, ATRX facilitates the restart of stalled replication forks, thereby promoting genome stability (Leung et al., 2013; Raghunandan et al., 2020).

In addition to the previously described partners, ATRX also interacts with several other proteins involved in stress response, heterochromatin maintenance, and homologous recombination, including RAD50, CtIP, RFC1, PCNA, ZNF274, TRIM28, and SETDB1 (Valenzuela et al., 2021).

Functional Partnership of ATRX and CTCF

CTCF (CCCTC-binding factor) is a highly conserved architectural protein that plays a central role in genome organization and transcriptional regulation. Structurally, it contains 11 zinc fingers that enable modular recognition of both core and flanking DNA motifs. Zinc fingers ZF3–ZF11 form direct contacts with the DNA major groove, while ZF1–ZF7 confer conformational flexibility, allowing CTCF to adapt to diverse genomic contexts and maintain high-affinity, sequence-specific binding (Yang et al., 2023).

Functionally, CTCF acts as a genomic insulator and transcriptional regulator, anchoring chromatin loops and establishing topologically associating domain (TAD) boundaries. This insulation restricts enhancer–promoter communication to defined domains, thereby preserving transcriptional specificity and preventing ectopic gene activation during development and differentiation (Ghirlando and Felsenfeld, 2016).

Live-cell imaging and polymer simulations have demonstrated that the Cohesin complex extrudes DNA to form chromatin loops, and that CTCF-binding sites act as directional barriers that halt extrusion when oriented convergently (Mach et al., 2022a). CTCF stabilizes loop anchors and defines TAD boundaries through its interaction with Cohesin, organizing the genome into reproducible three dimensional structures that regulate gene expression (Nora et al., 2020).

CTCF’s activity is epigenetically regulated, particularly by CpG methylation at its binding sites, which reduces occupancy and disrupts loop formation. During embryogenesis, dynamic changes in DNA methylation reshape CTCF-mediated chromatin architecture,

altering TAD boundaries and enhancer–promoter insulation, underscoring its sensitivity to epigenetic reprogramming and its role in developmental genome organization (Monteagudo-Sánchez et al., 2024). Beyond its architectural functions, CTCF contributes to DNA replication and repair by stabilizing nucleosome positioning after replication and facilitating homologous recombination at sites of genomic damage (Kang and Lee, 2021; Raimer Young et al., 2024).

Importantly, CTCF function is modulated by chromatin accessibility which is influenced by ATRX. In ATRX-deficient neonatal brains, nucleosome density is reduced, CTCF occupancy is disrupted at key regulatory loci, and chromatin loop formation is impaired, indicating that ATRX is required to maintain a chromatin environment conducive to CTCF binding and architectural function (Kernohan et al., 2014).

ATRX also cooperates with MeCP2 and Cohesin at imprinted loci such as H19/Igf2, where they regulate chromatin looping and gene silencing. This regulatory network further involves CTCF and the ERCC1–XPF DNA repair complex, linking chromatin architecture and DNA repair to epigenetic repression during neurodevelopment (Chatzinikolaou et al., 2017; Kernohan et al., 2010a).

In human cancer cells, ATRX loss causes global alterations in chromatin accessibility and transcription, directly impacting regulatory sites occupied by CTCF and compromising their functional integrity (Danussi et al., 2018; Liang et al., 2020a).

Moreover, in IDH-mutant glioma models and immunosuppressed tumor contexts, ATRX regulates glial identity and modulates the tumor microenvironment by influencing immune gene expression and chromatin accessibility at CTCF-occupied enhancers, suggesting a cooperative role in orchestrating transcriptional responses to environmental cues (Babikir et al., 2021; Diaz, 2022).
Finally, the histone variants H3.3 and H2A.Z co-occupy actively transcribed promoters and enhancers, including those bound by CTCF, where they contribute to a dynamic nucleosome landscape that facilitates transcription factor access (Chen et al., 2014).

Chromatin Organization

Chromatin organization is hierarchically structured into compartments, topologically associating domains (TADs), and chromatin loops, which together orchestrate the

spatial regulation of gene expression. At the largest scale, the genome segregates into A and B compartments, reflecting transcriptionally active and inactive regions, respectively, and these compartments are associated with distinct histone modifications, replication timing, and nuclear positioning (Zagirova et al., 2024). Within compartments, TADs represent megabase-sized domains of high internal contact frequency, demarcated by boundary elements enriched in CTCF and cohesin, which insulate regulatory interactions and maintain transcriptional fidelity (Hafner et al., 2023). At finer resolution, chromatin loops form between distal genomic elements such as enhancers and promoters, and are dynamically regulated by loop extrusion, a process in which cohesin translocates along DNA until halted by convergently oriented CTCF-binding sites (Mach et al., 2022b). These architectural layers are essential for maintaining genome integrity and cell-type-specific transcriptional programs. When disrupted, for example by loss of cohesin or CTCF, chromatin architecture becomes disorganized, leading to enhancer hijacking, ectopic gene activation, and transcriptional noise, which have been implicated in developmental disorders and cancer (Hafner et al., 2023; Zagirova et al., 2024).

AIM OF THE PROJECT

Numerous studies have suggested a potential functional interaction between ATRX and CTCF (Babikir et al., 2021; Chatzinikolaou et al., 2017; Kernohan et al., 2010b, 2014; Liang et al., 2020a), with some evidence showing a correlation between the deposition of the histone variant H3.3 and CTCF binding sites (Chen et al., 2014; Weth et al., 2014). However, these observations are often limited to specific gene loci, such as imprinted loci (Chatzinikolaou et al., 2017; Kernohan et al., 2014, 2010b), or to restricted cellular contexts, such as IDH-mutant gliomas, where changes in nucleosome density have been observed without detailed characterization of the histones involved

(Babikir et al., 2021; Liang et al., 2020b). Consequently, it remains unclear how ATRX regulates CTCF, and whether such regulation is locus-specific or genome-wide.

My project aims to address this gap by systematically analyzing the role of ATRX in the regulation of CTCF on a genome-wide scale, with the goal of clarifying if and how ATRX influences the three-dimensional chromatin architecture. To this end, I will use mouse embryonic stem cells (mESCs) as a model system, as they provide a physiological context free of oncogenic factors. The analysis will be performed using a highthroughput CUT&RUN approach, which allows high-resolution mapping of CTCF binding and histone variant deposition, both in wild-type and knockout ATRX conditions.

Understanding the link between ATRX and CTCF is highly relevant for elucidating the molecular mechanisms underlying ATR-X syndrome, as well as for interpreting the biology of solid tumors.

RESULTS

ATRX loss is accompanied by widespread CTCF and DNA methylation changes

To identify a global role, if any, for ATRX in CTCF localization, we examined CTCF genomic occupancy in WT and ATRX knock out (ATRX KO) mouse embryonic stem cells (mESCs). We found that CTCF protein levels are not changed upon ATRX loss (Figure1), and CTCF signal is not noticeably changed at the genome-wide level in ATRX KO mESCs (Figure 2). Previous studies have identified ATRX dependent regulation of CTCF occupancy at imprinted control regions (ICRs)(Kernohan et al., 2010b; Voon et al., 2015). We examined CTCF binding at imprinted loci and observed decreased CTCF upon ATRX loss at the majority of ICRs that are bound by CTCF in WT mESCs, in agreement with a role for ATRX in CTCF regulation at imprinted genes (Figures 3, 4).

Both H19 and Peg13 imprinted genes show CTCF enrichment in WT mESCs, which is lost in ATRX KO (Figure 4). Next, we performed differential binding analysis to identify genomic regions which showed significantly altered CTCF binding and found that out of 52,993 CTCF sites, 2,821 sites displayed increased CTCF, and 3,091 sites showed decreased CTCF binding in ATRX KO compared to WT (Figures 5, 6, and 7). These sets of gained and lost CTCF sites were both strongly enriched for the CTCF consensus motif (Figure 5), reinforcing that they are bona fide CTCF binding sites that become deregulated upon ATRX loss.

CTCF binding to its consensus motif can be affected by DNA methylation (MonteagudoSánchez et al., 2024). We first performed enhanced reducedrepresentation bisulfite sequencing (ERRBS) to measure DNA methylation changes between WT and ATRX KO mESCs and discovered global hypomethylation in ATRX KO cells (Figure 8), with the extent of hypomethylation greatest in regions with high DNA methylation in WT cells (Figure 9). Interestingly, transient knockdown of ATRX (ATRX KD) for 72 hours revealed no significant changes in DNA methylation (Figures 10,11,12). Similarly, we did not observe differentially regulated CTCF sites in ATRX KD mESCs (Figure 13), suggesting that the changes seen in methylation and CTCF abundancy accumulate over time.

Next, we identified 9,313 CTCF peaks that were represented in ERRBS data and examined whether CTCF redistribution in ATRX KO could be attributed to changes in DNA methylation. Analysis of the 715 sites with significant loss of CTCF showed that most of these lost sites did not show a substantial change in DNA methylation (Figure 14, left, blue dots and Figure 15). In contrast, a greater proportion of sites which gain CTCF sites showed decrease in DNA methylation (Figure 14, right, red dots and Figure 15). Quantification of DNA methylation differences across gained, lost, and invariant CTCF sites showed a clear shift toward hypomethylation at gained CTCF sites, but not lost or invariant sites (Figure 16). Our results indicate that CTCF losses in ATRX KO are largely DNA methylation independent, while CTCF gains are more correlated with CpG hypomethylation.

ATRX binds the histone H3 tail that is di- or tri-methylated at lysine 9 (H3K9me2/3) (Argentaro et al., 2007; Dhayalan et al., 2011; Eustermann et al., 2011b; Iwase et al.,

2011) and this interaction serves to maintain H3K9 methylation at specific genomic sites (Valle-García et al., 2016). Histone H3K9 methylation dependent DNA methylation was reported in plants and filamentous fungi (Jackson et al., 2002; Law and Jacobsen, 2010; Tamaru et al., 2003; Tamaru and Selker, 2001). Recent studies interrogating the relationship between H3K9me3 and DNA methylation in mammalian cells showed that the DNA methyltransferase enzyme DNMT1 interacts with H3K9me3, which results in the enhanced activity of DNMT1 (Ren et al., 2020). Consequently, abolishing the interaction between DNMT1 and H3K9me3 resulted in reduced global DNA methylation. Analysis of histone modification patterns in WT and ATRX KO mESCs showed that H3K9me2 and H3K9me3 were significantly depleted in ATRX KO (Figure 16), which could partly explain decreased DNA methylation in the long run. Together, our findings indicate that long-term ATRX deficiency results in profound and genome-wide dysregulation of both CTCF localization and DNA methylation.

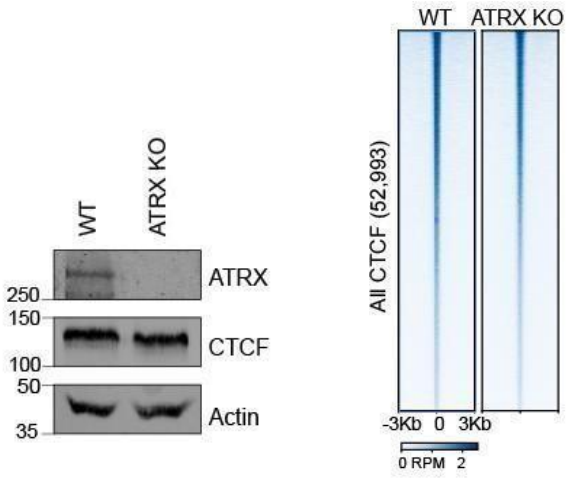

Fig. 1 Western blot for ATRX, CTCF, and actin in wildtype and ATRX KO mESCs. Antibodies are indicated on the right. **Fig. 2** Heatmap of RPM-normalized CTCF CUT&RUN signal in wildtype and ATRX KO mESCs across 52,993 consensus CTCF peaks called across wildtype and ATRX KO. RPM, reads per million. **Fig. 3** Scatter plot of log2 CTCF read density (reads per million, RPM) in wildtype and ATRX KO mESCs across

52993 CTCF peaks. Each point represents an individual peak, with red dots highlighting CTCF peaks that overlap known imprinted control regions.

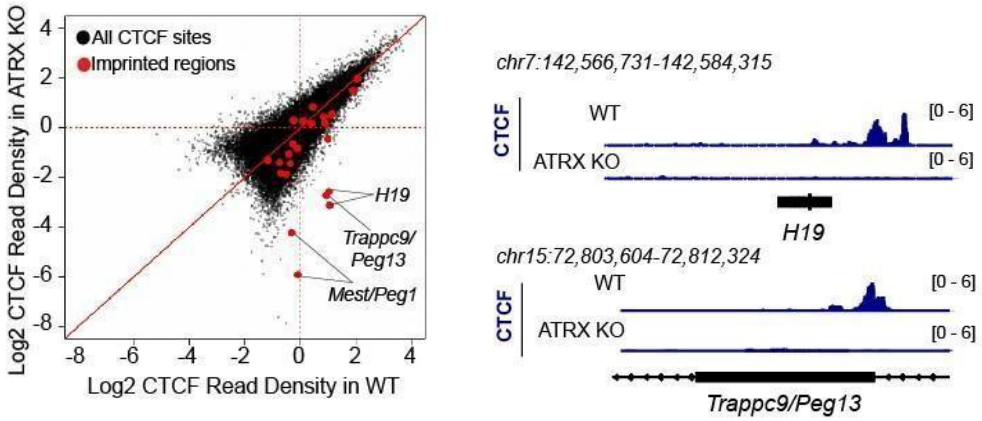

Fig. 3 Scatter plot of log2 CTCF read density (reads per million, RPM) in wildtype and ATRX KO mESCs across 52993 CTCF peaks. Each point represents an individual peak, with red dots highlighting CTCF peaks that overlap known imprinted control regions. **Fig. 4** Genome browser view of the *H19* and *Trappc9* imprinting control regions showing RPM-normalized CTCF CUT&RUN signal in wildtype and ATRX KO mESCs.

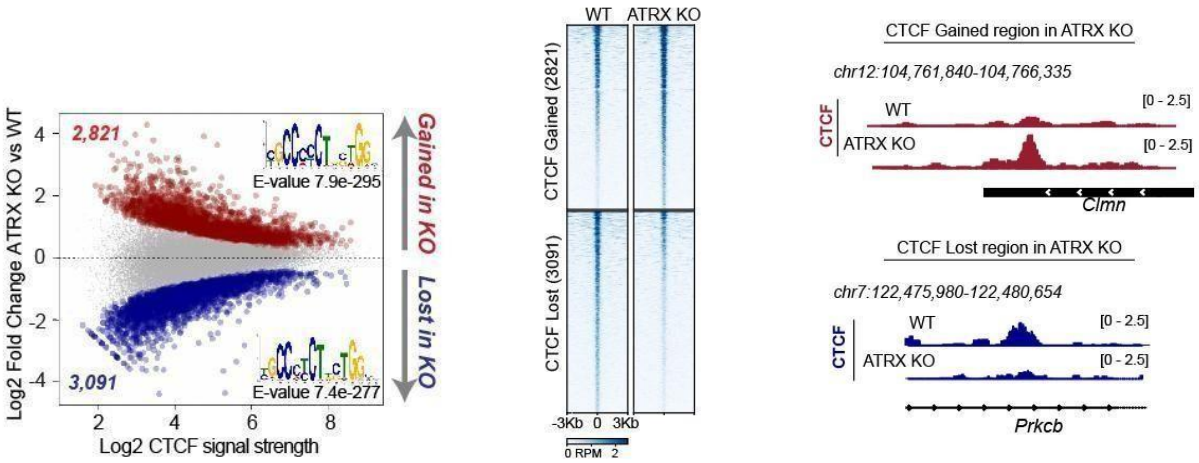

Fig. 5 MA plot of differential CTCF binding between wildtype and ATRX KO mESCs showing average normalized signal intensity on the x-axis and log2 fold change on the y-axis. Peaks with significantly increased or decreased CTCF binding in ATRX KO (FDR <= 0.05) are highlighted in red and blue, respectively. CTCF motifs identified by motif analysis of gained and lost sites are indicated**. Fig. 6** Heatmap of CTCF CUT&RUN signal across 2,821 gained and 3,091 lost CTCF peaks in wildtype and ATRX KO mESCs. RPM, reads per million**. Fig.7** Genome browser view of the *Clmn* and *Prkcb* genes showing RPMnormalized CTCF CUT&RUN signal in wildtype and ATRX KO mESCs, representing gained and lost CTCF peaks.

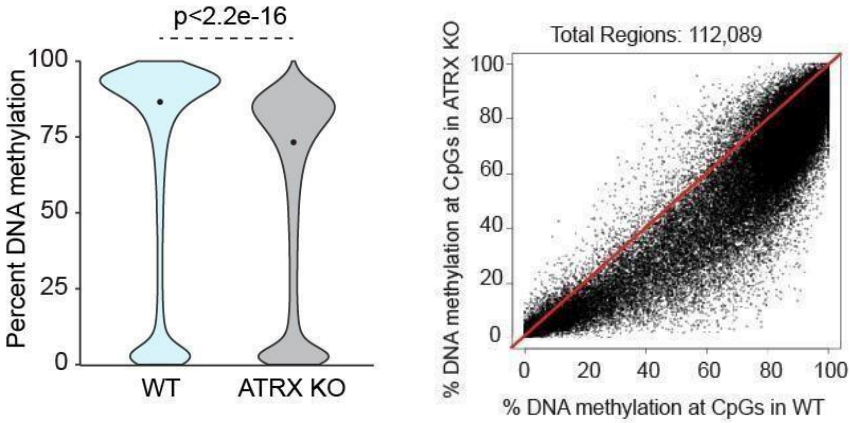

Fig. 8 Violin plot of CpG methylation levels in wildtype and ATRX KO mESCs. p-value, Welch's two-sided t-test. **Fig. 9** Scatter plot of 1-kb tiled genomic windows showing mean CpG methylation in wildtype and ATRX KO mESCs. Methylation levels were calculated by computing mean methylation of all CpGs within each window.

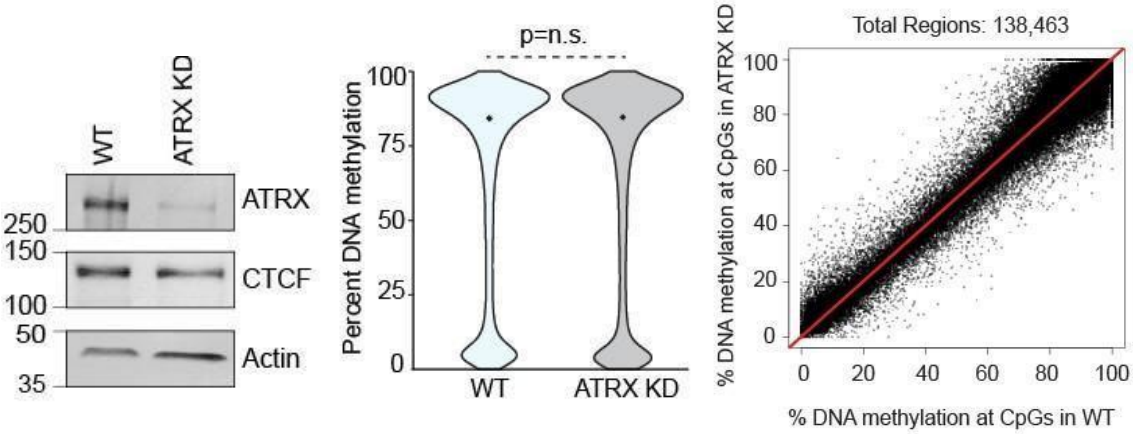

Fig. 10 Western blot for ATRX, CTCF, and actin in wildtype and ATRX knockdown mESCs. Antibodies are indicated on the right. **Fig. 11** Violin plot of CpG methylation levels in wildtype and ATRX knockdown mESCs. p-value, Welch's two-sided t-test. **Fig. 12** Scatter plot of 1-kb tiled genomic windows showing mean CpG methylation in wildtype and ATRX knockdown mESCs. Methylation levels were calculated by computing mean methylation of all CpGs within each window.

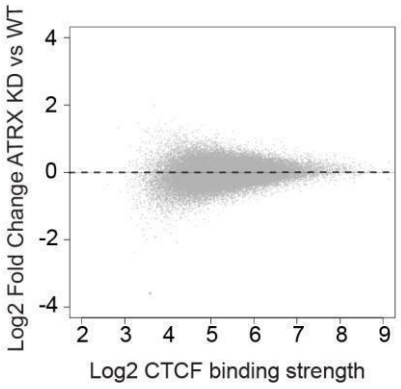

Fig.13 MA plot of differential CTCF binding between wildtype and ATRX knockdown mESCs showing average normalized signal intensity on the x-axis and log2 fold change on the y-axis. No significantly changed peaks (FDR <= 0.05) were identified.

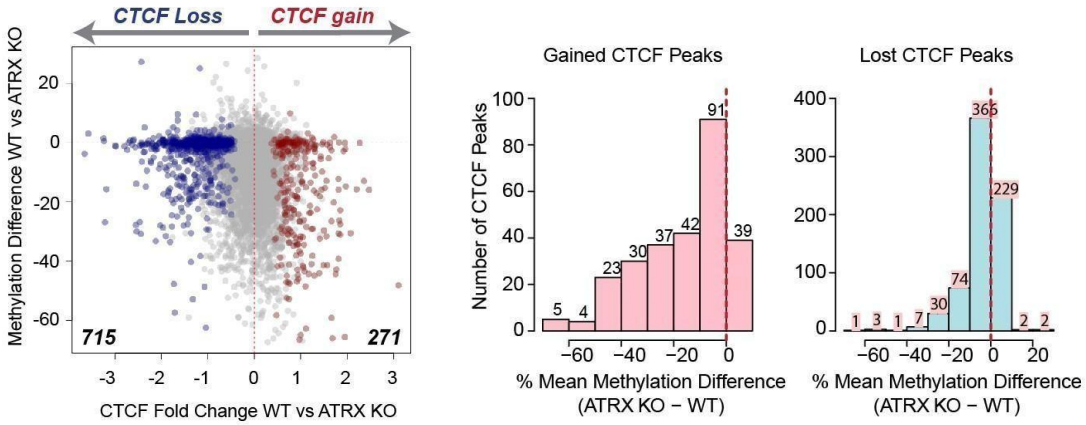

Fig. 14 Scatter plot showing log2 fold change in CTCF binding between wildtype and ATRX KO mESCs on the x-axis, versus mean CpG methylation difference between wildtype and ATRX KO mESCs on the y-axis, across 9,313 CTCF peaks that contains CpGs covered by ERRBS. 715 significantly lost CTCF peaks and 271 gained CTCF peaks (FDR <= 0.05) are highlighted in blue and red, respectively., representing gained and lost CTCF peaks. **Fig. 15** Histogram of mean methylation difference between wildtype and ATRX KO mESCs across gained and lost CTCF peaks, showing methylation difference on the x-axis and the number of peaks on the y-axis.

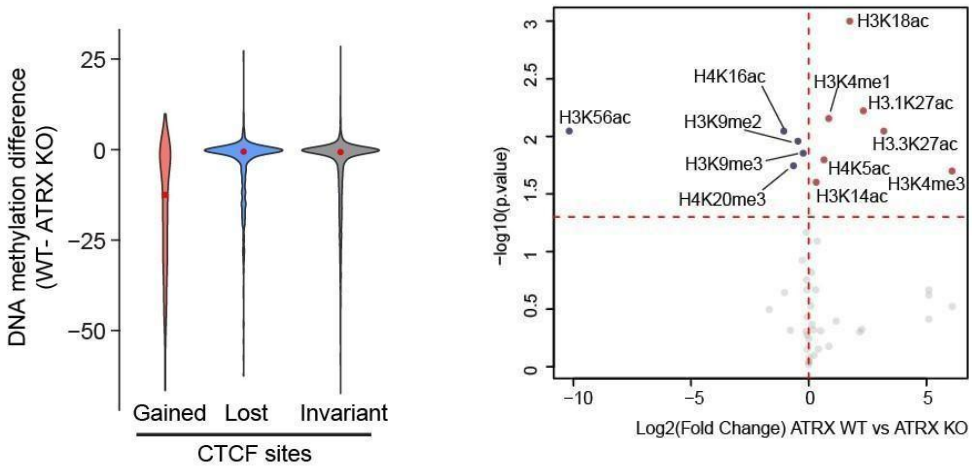

Fig 16 Histogram of mean methylation difference between wildtype and ATRX KO mESCs across gained and lost CTCF peaks, showing methylation difference on the x-axis and the number of peaks on the y-axis.
Fig 17 Volcano plot of histone mark mass spectrometry results showing log2 fold change on the x-axis and –log10 p-value on the y-axis. Histones showing significant increase or decrease in ATRX KO mESCs compared to wildtype are highlighted in red and blue, respectively.

CTCF alterations in ATRX deficient cells is linked to changes in H3.3 deposition

CTCF binding sites are enriched for the histone variant H3.3 (Jin et al., 2009; Weth et al., 2014). We confirmed genomic co-localization of CTCF and H3.3 in mESCs and a depletion of the H3K27me3 mark at CTCF sites (Figures 17 and 18) (Weth et al., 2014). Next, we examined CTCF genomic occupancy in mESCs knocked down for H3.3 (Figure 19) and observed a genome-wide reduction in CTCF binding in H3.3 KD (Figure 20). Furthermore, at CTCF sites lost in ATRX KO, the extent of CTCF loss was well correlated between H3.3 KD and ATRX KO (Figure 21). ATRX plays a critical role in regulating deposition of H3.3 as part of the ATRX/DAXX complex (Drané et al., 2010; Goldberg et al., 2010) at repetitive genomic regions. We examined CTCF localization in

DAXX KO mESCs (Figure 22) and found that as with H3.3 KD, CTCF binding was globally reduced (Figure 23). Accordingly, CTCF behavior in DAXX KO closely resembled that in ATRX KO (Figures 24, 25) and H3.3 KD (Figure 26, 27).

We next re-examined our significantly gained and lost CTCF sites in ATRX KO mESCs (Figure 5) in the context of H3.3. We reasoned that if H3.3 occupancy positively regulates CTCF binding, sites which gain CTCF in ATRX KO would show higher H3.3 levels while sites that lose CTCF would show reduced H3.3. Analysis of H3.3 enrichment at 2,821 gained and 3,091 lost CTCF sites revealed exactly this pattern, with H3.3 levels significantly increased at sites where CTCF is gained in ATRX KO and decreased at lost CTCF sites (Figure 28). We also examined the relationship between H3.3 and DNA methylation and found that at regions which gain CTCF, sites with decreased DNA methylation are also enriched for H3.3 (Figure 29). In contrast, this positive correlation is absent at regions that lose CTCF (Figure 30). Therefore, ATRXmediated changes in CTCF occupancy is regulated in large part through effects on H3.3 deposition.

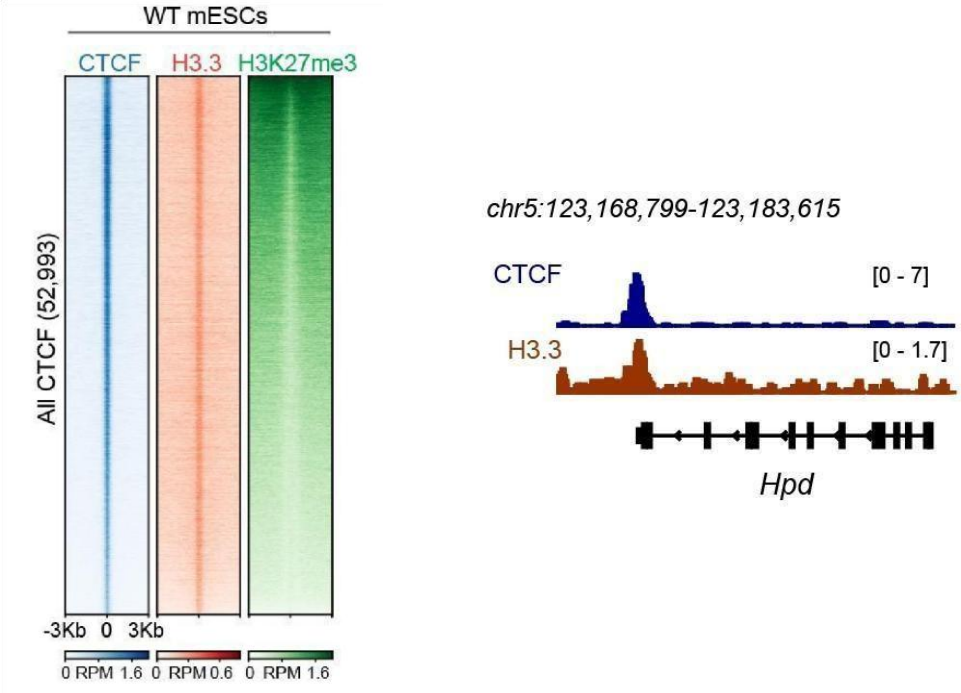

Fig. 17 Heatmap of RPM-normalized CTCF and H3.3 CUT&RUN and H3K27me3 ChIP-seq signal in wildtype mESCs across 52,993 consensus CTCF peaks called across wildtype and ATRX KO. RPM, reads per million.**Fig. 18** Genome browser view of the Hpd gene showing RPM-normalized CTCF and H3.3 CUT&RUN signal in wildtype mESCs.

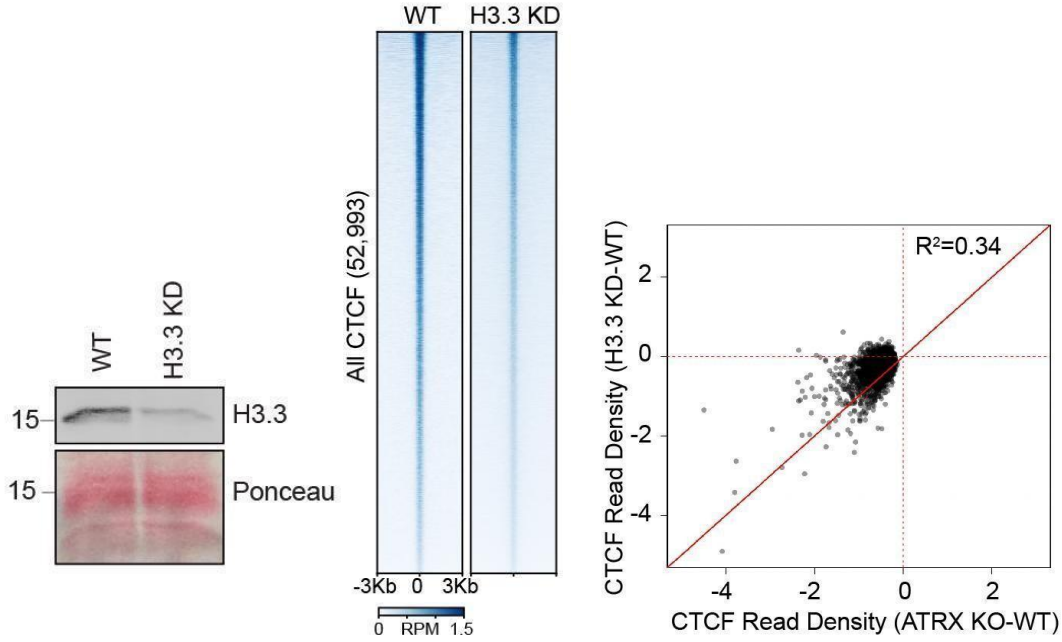

Fig. 19 Western blot analysis for H3.3 in acid extracted histones from wildtype and H3.3 KD mESCs. Ponceau staining was used as a loading control. **Fig. 20** Heatmap of RPM-normalized CTCF CUT&RUN signal in wildtype and H3.3 KD mESCs across 52,993 consensus CTCF peaks called across wildtype and ATRX KO. RPM, reads per million. **Fig. 21** Scatter plot comparing difference in CTCF read density between wildtype and ATRX KO on the x-axis, and between wildtype and H3.3 KD on the y-axis, across 3,091 CTCF peaks lost in ATRX KO.

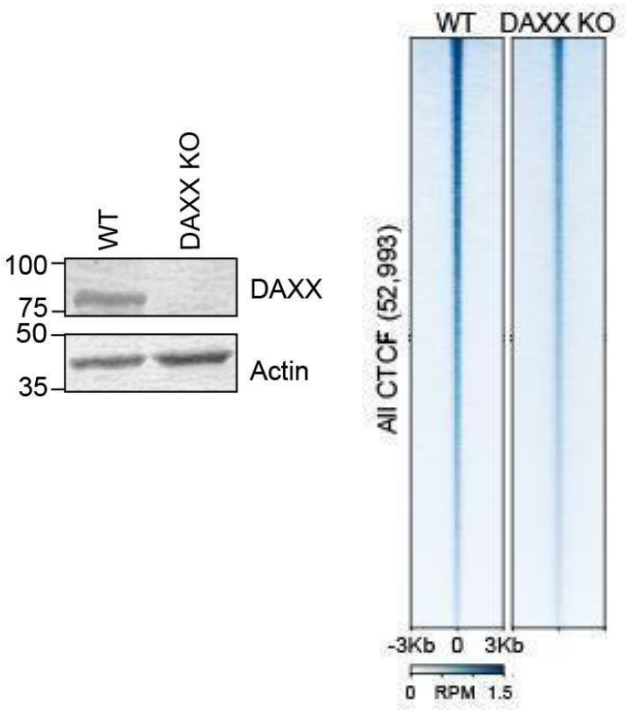

Fig.22 Western blot for DAXX and actin in wildtype and DAXX KO mESCs. Antibodies are indicated on the right. **Fig.23** Heatmap of RPM-normalized CTCF CUT&RUN signal in wildtype and DAXX KO mESCs across 52,993 consensus CTCF peaks called across wildtype and ATRX KO. RPM, reads per million.

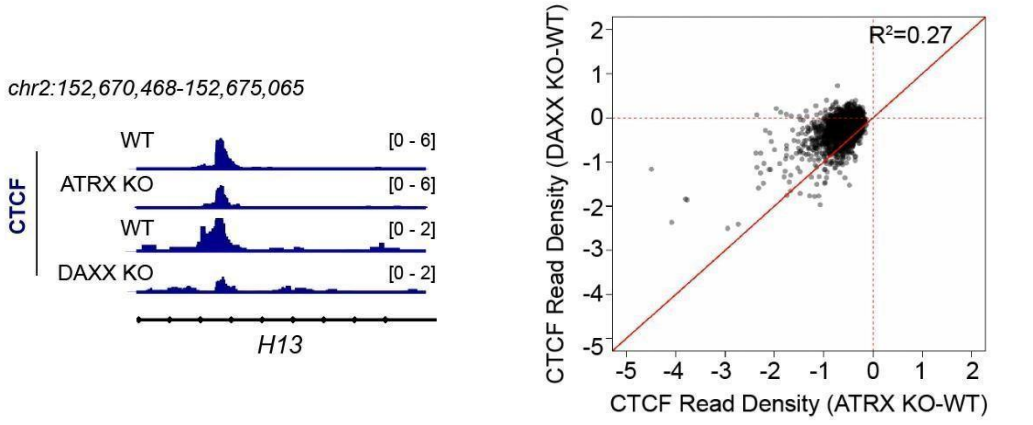

Fig 24 Genome browser view of the H13 gene showing RPM-normalized CTCF CUT&RUN signal in

ATRX KO, DAXX KO, and matched wildtype mESCs. **Fig 25** Scatter plot comparing difference in CTCF read density between wildtype and ATRX KO on the x-axis, and between wildtype and DAXX KO on the yaxis, across 3,091 CTCF peaks lost in ATRX KO.

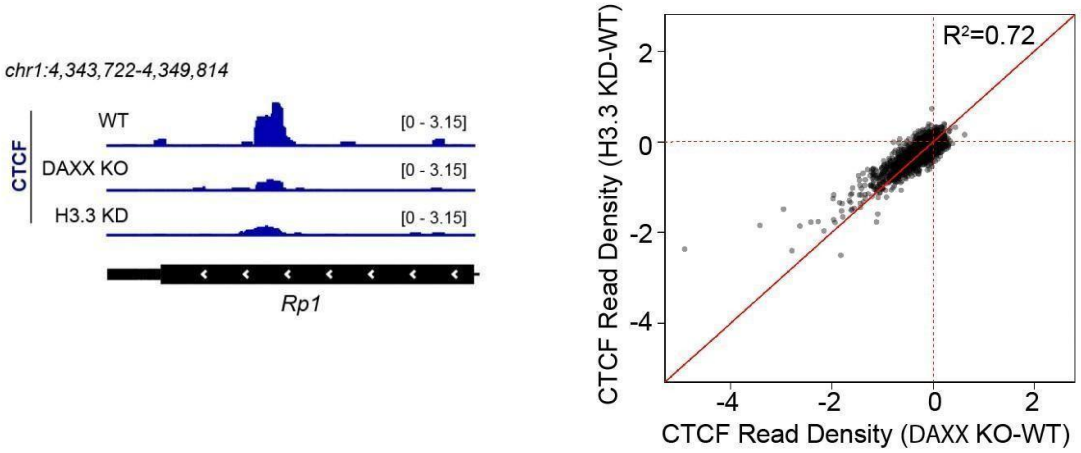

Fig. 26 Genome browser view of the Rp1 gene showing RPM-normalized CTCF CUT&RUN signal wildtype, DAXX KO, and H3.3 KD mESCs. **Fig. 27** Scatter plot comparing difference in CTCF read density between wildtype and DAXX KO on the x-axis, and between wildtype and H3.3 KD on the y-axis, across 3,091 CTCF peaks lost in ATRX KO.

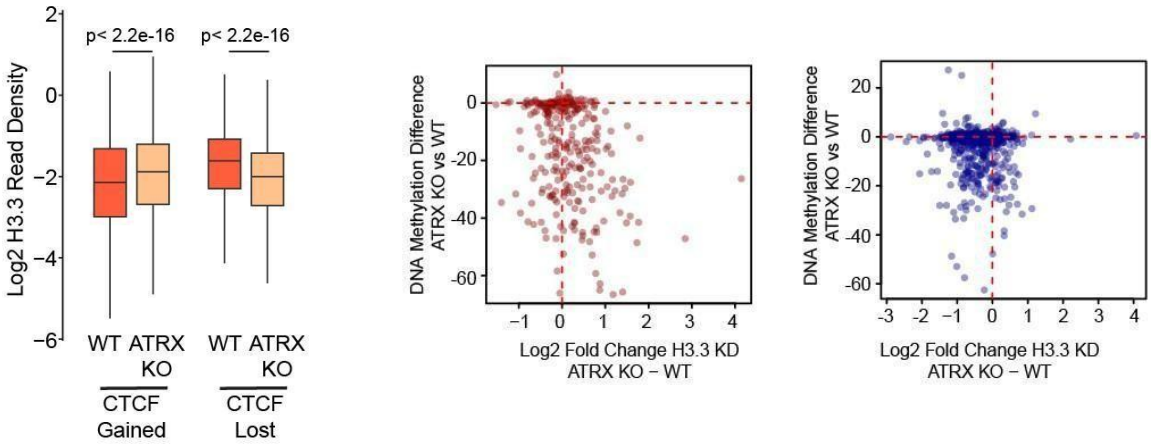

Fig. 28 Boxplot of log2 H3.3 read density (RPM, reads per million) in wildtype and ATRX KO mESCs at gained and lost CTCF sites. p-values, Welch's two-sided t-test. Box, 25th percentile, median, and 75th percentile. Whiskers extend to 1.5x interquartile range; outliers not displayed. **Fig. 29** Scatter plot of significant CTCF gained regions (FDR < 0.05) showing H3.3 read density fold change in ATRX KO versus WT on the x-axis and DNA methylation difference on the y-axis. **Fig 30** Scatter plot of significant CTCF lost regions (FDR < 0.05), showing H3.3 read density fold change in ATRX KO versus WT on the x-axis and DNA methylation difference on the y-axis.

HIRA histone chaperone complex is redistributed genome-wide upon ATRX loss

The ATRX/DAXX complex is well-established to deposit H3.3 at repetitive regions of the genome (Law et al., 2010; Sadic et al., 2015b; Wong et al., 2010). H3.3 deposition at active or repressed genes and other euchromatic sites is primarily mediated by the HIRA histone chaperone complex (Goldberg et al., 2010). While a recent study indicated that ATRX localizes to many euchromatic regions containing transcription factor binding sites, CTCF sites were not abundantly represented (Truch et al., 2022). While a recent study indicated that ATRX localizes to many euchromatic regions containing transcription factor binding sites, CTCF sites were not abundantly represented (Lynskey et al., 2024). In this scenario, HIRA is redirected to telomeres in the absence of ATRX-DAXX to maintain H3.3 levels at these regions, which contributes to telomere compaction and repression. Thus, we hypothesized that in mESCs, which naturally contain long telomeres, ATRX loss results in redistribution of HIRA away from euchromatic targets, including promoters and CTCF sites, to telomeres. To test this, we examined genome-wide HIRA localization in WT and ATRX KO mESCs. Peak calling identified 651 HIRA binding sites in WT mESCs across 2 replicates. Analysis of HIRA enrichment across these sites showed that HIRA binding becomes significantly weaker in ATRX KO cells (Figures 31 and 32). We next examined HIRA enrichment at sites that gain and lose CTCF in ATRX KO. HIRA signal decreases at regions with reduced CTCF binding (Figure 33, left), but increased at CTCF gained sites (Figure 33, right), suggesting that HIRA is redistributed away from its endogenous targets towards a different subset of genomic loci upon ATRX loss.

Next, we sought to identify characteristics of gained CTCF sites that might contribute to increased HIRA localization. Several epigenetic mechanisms contribute to repression of endogenous retroviruses (ERVs), which are flanked by long terminal repeat (LTRs) elements and that when activated can result in genome instability (Elsässer et al., 2015a; Matsui et al., 2010; Walsh et al., 1998; Wolf et al., 2015; Yang et al., 2015). ATRX plays an important role in repressing endogenous retroviruses and loss of ATRX was shown to increase ERV expression (Sadic et al., 2015b). To test whether HIRA is drawn to genomic regions containing ERVs, we examined the prevalence of LTRs at CTCF gained and lost sites in ATRX KO. We found that 27.8% of sites that gained CTCF also contained an LTR, representing a 1.67-fold enrichment over background (hypergeometric test, p-value = 8.35 x 10-53), compared to only 15.8% of lost CTCF sites (Figure 34). Furthermore, binding of both HIRA and H3.3 is significantly higher at CTCF gained sites containing LTRs than at gained sites lacking LTRs (Figures 35 and 36). These results suggests that in the absence of ATRX, HIRA redistribution may be triggered to ensure continued repression of specific repetitive regions through the deposition of H3.3. When H3.3 accrual occurs over CTCF motifs, this could produce a chromatin environment conducive to increased CTCF binding. Conversely, CTCF is lost from motifs where H3.3 levels are reduced because of HIRA relocation away from its usual targets (1st model).

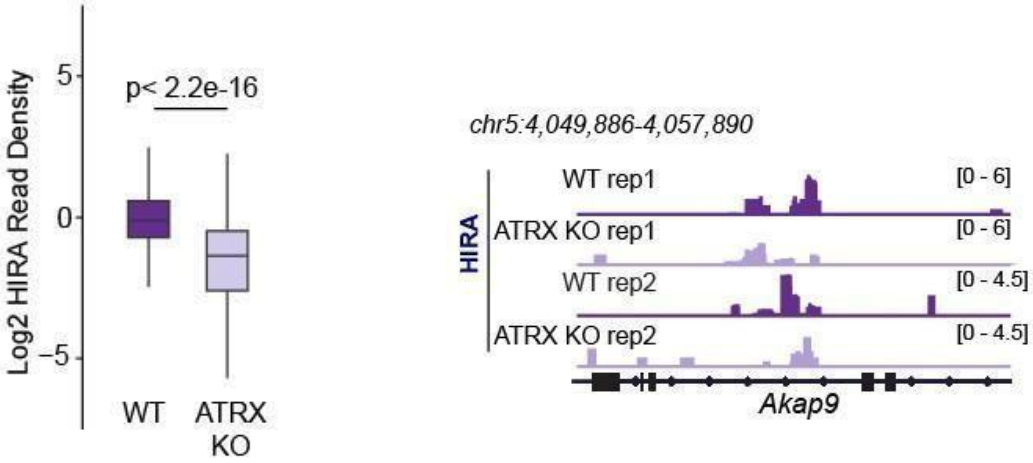

Fig. 31 Boxplot of log2 HIRA read density (RPM, reads per million) in wildtype and ATRX KO mESCs across HIRA peaks called from individual HIRA CUT&RUN replicates of wildtype mESCs. p-values, Welch's twosided t-test. Box, 25th percentile, median, and 75th percentile. Whiskers extend to 1.5x interquartile range; outliers not displayed. **Fig. 32** Genome browser view of the Akap9 gene showing RPM-normalized HIRA CUT&RUN signal in wildtype and ATRX KO mESCs.

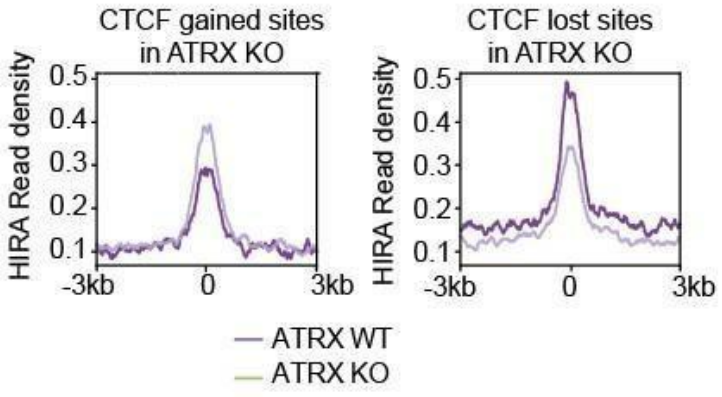

Fig. 33 Profile plot of RPM-normalized HIRA read density in wildtype and ATRX KO mESCs across gained and lost CTCF sites.

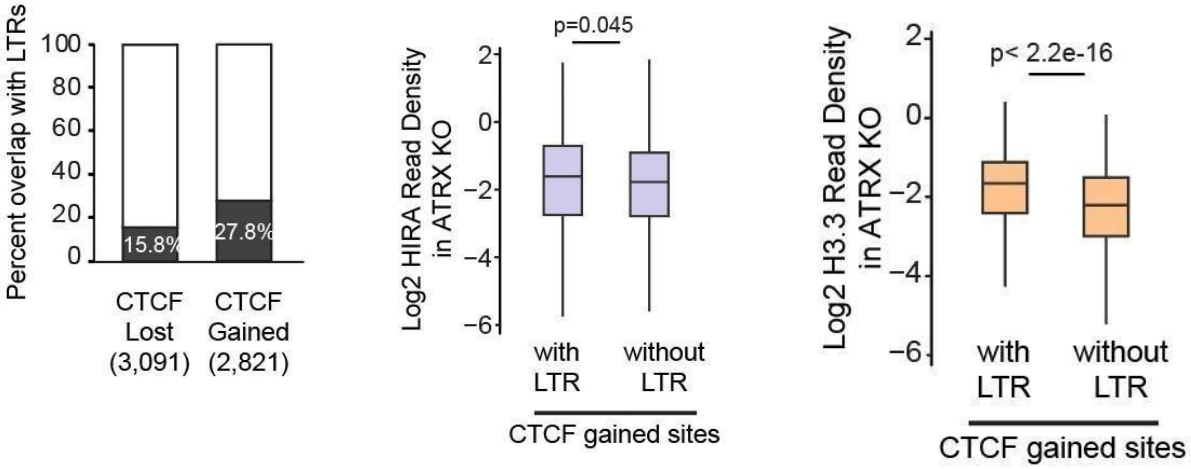

Fig. 34 Barchart showing the percentage of lost and gained CTCF peaks overlapping long terminal repeat (LTR) elements. **Fig. 35** Boxplot of log2 HIRA read density (RPM, reads per million) in ATRX KO mESCs across CTCF peaks overlapping long terminal repeat (LTR) elements and non-overlapping LTR. Welch's two-sided t-test. Box, 25th percentile, median, and 75th percentile. Whiskers extend to 1.5x interquartile range; outliers not displayed. **Fig. 36** Boxplot of log2 H3.3 read density (RPM, reads per million) in ATRX KO mESCs across

CTCF peaks overlapping long terminal repeat (LTR) elements and non-overlapping LTR. Welch's two-sided t-test. Box, 25th percentile, median, and 75th percentile. Whiskers extend to 1.5x interquartile range; outliers not displayed

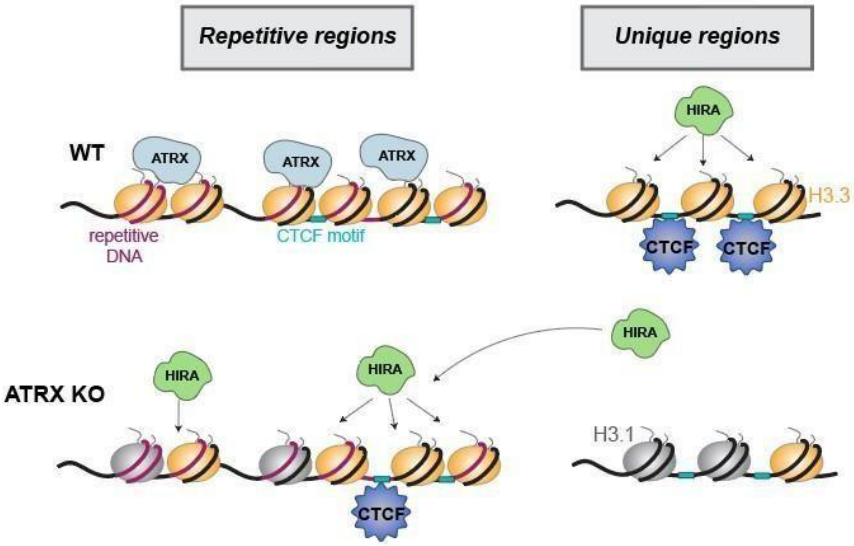

1st model Model for ATRX-mediated regulation of CTCF. Top - ATRX-DAXX complex deposits histone H3.3 at repetitive heterochromatic regions, while HIRA deposits H3.3 at unique euchromatic sites. High H3.3 levels around CTCF motifs facilitate CTCF binding. Bottom – Upon ATRX loss, HIRA is relocated from euchromatin to repetitive regions, including transposable elements, to maintain H3.3 levels and ensure repression. CTCF gains and losses follow H3.3 changes on chromatin.

ATRX loss blurs genome-wide replication timing and A/B compartmentalization

Our results show that ATRX loss alters the genome-wide binding of the chromatin architectural protein CTCF. To determine the consequences of CTCF changes on higher-order genome organization, we performed Hi-C in WT and ATRX KO mESCs. Visualization of Hi-C chromosome contact maps show typical checkerboard patterns in WT mESCs (Figures 37 and 38). Interestingly, this pattern was eroded across all chromosomes in ATRX KO mESCs (Figures 37,38,39) indicating profound changes in A/B compartmentalization across the genome. We ordered and binned regions by

eigenvector (Figure 37, bottom right) to examine interactions between compartments genome-wide and found that the frequency of interactions between A and B compartments was increased in ATRX KO (Figure 40, top-left and bottom-right corners), consistent with blurring of A and B compartment definitions.

We computed principal components of 100kb-resolution Hi-C data (Figure 3A, bottom right) to more closely examine changes in compartmentalization upon ATRX loss. Our analysis identified 1,900 regions across the genome that underwent statistically significant compartmental changes in ATRX KO mESCs (Figure 41). Of these, we identified 908 regions (47.8%) as “B-to-A” flipping compartments that were defined as B compartments in WT but as A compartments in ATRX KO. Meanwhile 394 (20.7%) “Ato-B” regions defined as A compartments in WT changed to B in ATRX KO. The remainder of compartments with significant changes in ATRX KO did not flip but were either strengthened or weakened in their compartmentalization compared to WT. However, previous studies have established that CTCF depletion in mESC using degron models is not accompanied by compartment level changes (Nora et al., 2017), prompting us to investigate other potential mechanisms that might underlie compartment erosion upon ATRX loss.

ATRX loss is associated with replication stress and genome instability (Teng et al., 2021; Wang et al., 2019). The most significantly depleted histone modification mark in ATRX KO mESCs is H3K56Ac (Figure 17), which is associated with DNA replication (Duan et al., 2025), in agreement with ATRX loss leading to delays in S phase progression. During DNA replication, the genome is organized into early and late replicating regions that correlate strongly with A/B compartmentalization (Ryba et al., 2010; Sima et al., 2019). Therefore, one possible explanation for the effect of ATRX loss on compartment changes is an alteration in replication timing resulting from increased replication stress. To examine the effect of ATRX loss on replication timing, we performed Repli-Seq (Marchal et al., 2018) to identify early and late replicating regions in WT and ATRX KO mESCs. We calculated log2 early/late (E/L) ratios across the genome in 50-kb bins, with an E/L ratio above 0 corresponding to early replicating regions (Figure 42, blue) and a ratio below 0 corresponding to late replicating regions (Figure 42, red). When comparing E/L ratios between WT and ATRX KO, we observed

that many regions deviate away from the diagonal indicating a shift in replication timing (Figure 43). This is especially apparent when we examine replication timing of bins within compartments that change from B to A (Figure 42 top, Figure 44, left). In WT, these compartments are clearly late replicating as evidenced by strongly negative E/L ratios. However, in ATRX KO, ratios are shifted upwards towards zero suggesting that these compartments, while still late replicating, now tend to replicate earlier in ATRX KO. We also examined A-to-B flipping compartments and found that their E/L ratios in WT were not skewed in either a positive or negative direction, suggesting these compartments may not be specifically associated with early or late replication timing (Figure 44, right). Nevertheless, in ATRX KO, E/L ratios were overall closer to zero in these regions. Together, these data indicate that while relatively few regions flip entirely from early to late replicating or vice versa, ATRX loss results in a general loss in coordination of early versus late replication events, which may contribute to the compartmentalization changes observed in ATRX KO mESCs.

DNA methylation plays a role in the regulation of both replication timing and compartmentalization (Du et al., 2021a). Knockout of DNA methyltransferases DNMT1 and DNMT3B resulted in blurring of compartment identity and replication timing domains, similar to what we observe upon ATRX loss. While methylation is decreased across the genome in ATRX KO, we found a significantly greater degree of hypomethylation at CpGs falling within B-to-A flipping compartments (Figure 45). Our results suggest that compartment level changes that accompany ATRX loss may occur due to changes in DNA methylation and replication timing.

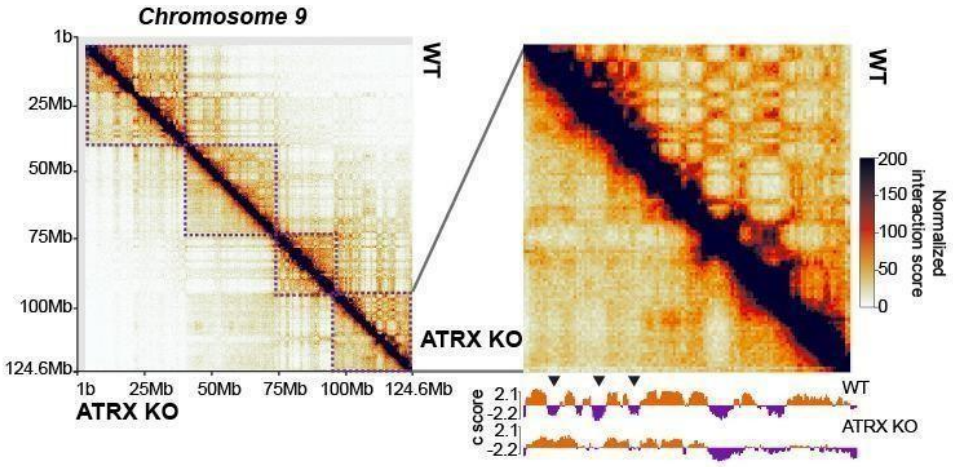

Fig. 37 Left, 250-kb resolution Hi-C map of chromosome 9, showing observed contacts in wildtype (upper right triangle) and ATRX KO (lower left triangle) mESCs. Right, inset of Hi-C map and PC1 plots of inset region indicating compartmentalization. Black triangles indicate B compartments in WT (negative PC1 value) that become A compartment-like in ATRX KO (near-zero or positive PC1 value).

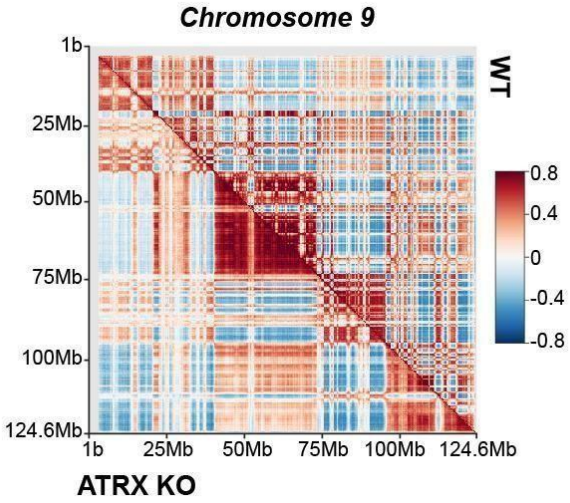

Fig. 38 250-kb resolution eigenvector plot of chromosome 9 showing A/B compartmentalization in wildtype (upper right triangle) and ATRX KO (lower left triangle) mESCs.

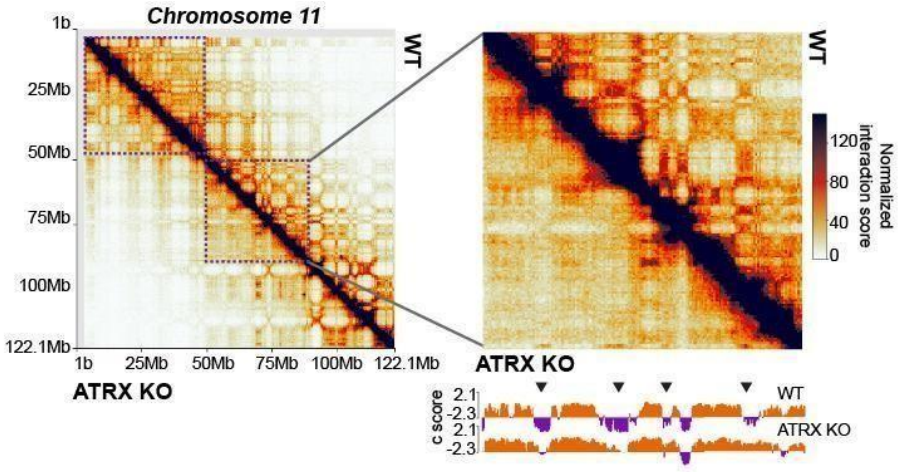

Fig. 39 Left, 250-kb resolution Hi-C map of chromosome 11, showing observed contacts in wildtype (upper right triangle) and ATRX KO (lower left triangle) mESCs. Right, inset of Hi-C map and PC1 plots of inset region indicating compartmentalization. Black triangles indicate B compartments in WT (negative PC1 value) that become A compartment-like in ATRX KO (near-zero or positive PC1 value).

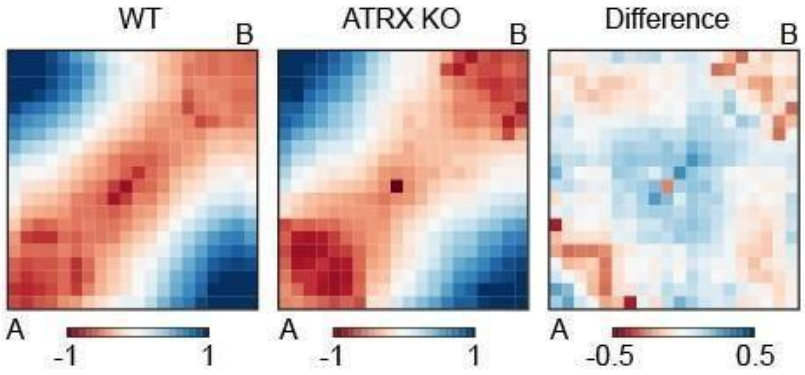

Fig. 40 Saddle plots of A and B compartments in wildtype and ATRX KO mESCs. Eigenvector values for 250kb genomic regions were ordered and binned by percentile and interactions between binned regions were compared to expected. Right-most plot represents the difference in O/E value between ATRXKO and wildtype saddle plots per pixel (ATRX KO – WT).

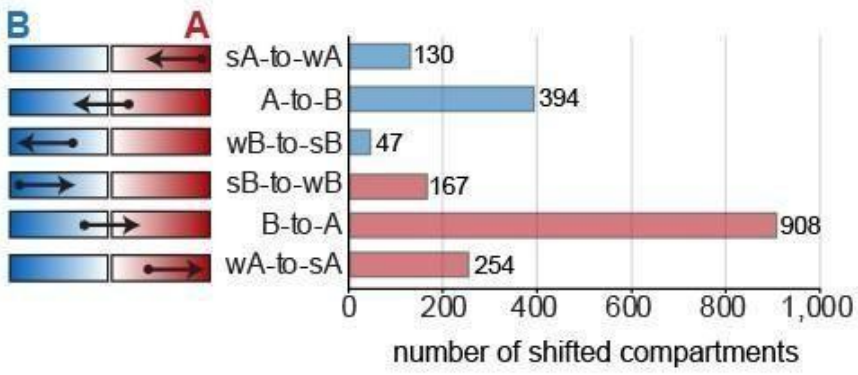

Fig. 41 Plot of 100-kb genomic regions that undergo statistically significant compartment shifts in ATRX KO mESCs compared to wildtype. Regions are grouped into those that remain A or B but shift from strong to weak (sA-to-wA, sB-to-wB) or weak to strong (wA-to-sA, wB-to-wB), or those that flip in compartment identity (A-to-B, B-to-A

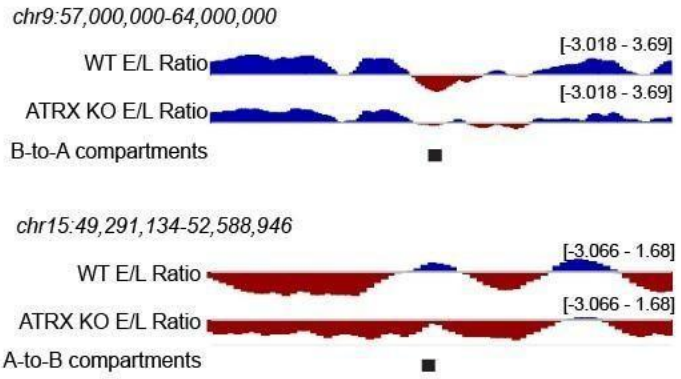

Fig. 42 Genome browser views of two regions on chromosome 9 and 15 showing replication timing (log2 early/late ratio) in wildtype and ATRX KO mESCs. Blue signal (E/L ratio > 0) indicates early replicating DNA, while red signal (E/L ratio < 0) indicates late replicating regions. Compartments that undergo B-to-A or A-to-B switches are highlighted.

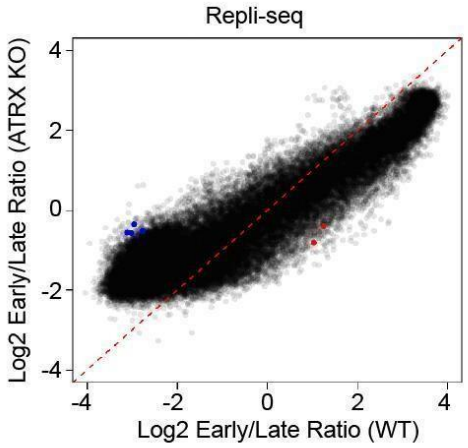

Fig. 43 Scatterplot showing replication timing (measured as log2 early/late ratio from Repli-Seq data) in wildtype and ATRX KO mESCs across 50-kb genomic windows. (work in progress)

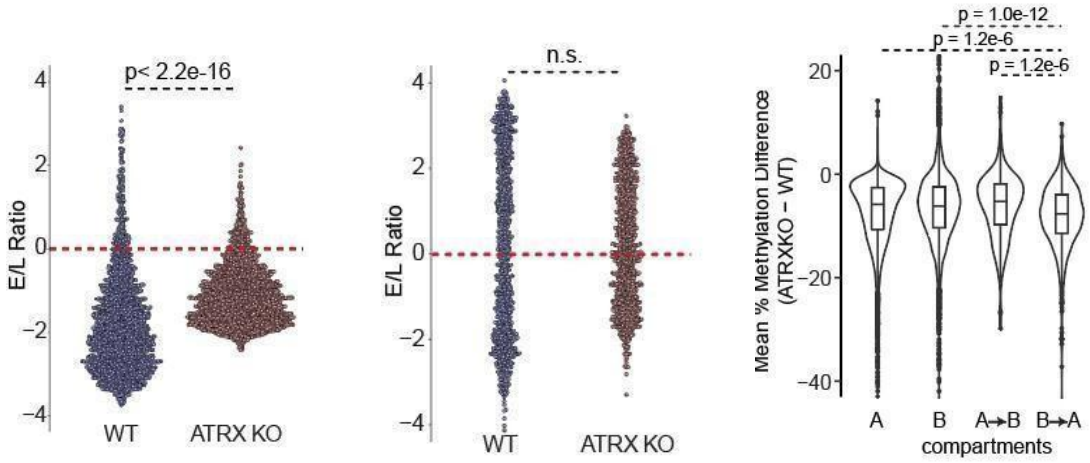

Fig 44. (Work in progress) **Fig 45.** Violin and boxplot of mean methylation difference between ATRX KO and wildtype mESCs of CpGs that fall within A, B, A-to-B, or B-to-A compartments. Box, 25th percentile – median – 75th percentile. Whiskers extend to 1.5x interquartile range. (work in progress p value)

ATRX loss alters topologically associated domain and chromatin loop organization through CTCF

Having found large-scale changes in A/B compartmentalization, we next examined differences in organization of TADs that delineate self-interacting sections of the genome, as well as chromatin loops that can facilitate gene expression (Bonev and

Cavalli, 2016). We performed TAD finding with OnTAD (An et al., 2019) to allow identification of TADs nested at different levels of hierarchical structure and genomic size (Figure 47, left) and found that the number of TADs increased upon (8,755 in ATRX KO compared to 7,947 in WT; Figure 46). size TADs were retained (Figure 48, top, black arrows). This loss of large TADs was accompanied by the formation of small TADs nested within medium-size TADs (Figure 48, bottom, black arrows), with interactions decreasing over the largest TADs while concentrating within the smaller TADs. On a genome-wide scale, this change in TAD organization was evidenced by a marked shift in TAD width (Figure 49), as ATRX KO mESCs have a lower frequency of large megabase-scale TADs and a higher frequency of small TADs in the 150kb to 300kb range (Figure 50). In terms of hierarchal structure, the largest level 1 TADs in WT mESCs often split into several smaller level 1 TADs in ATRX KO, resulting in altered nesting. Accordingly, each level of TAD was consistently smaller in width in ATRX KO mESCs compared to WT (Figure 47, right), confirming that ATRX loss results in breakdown of larger TADs genome-wide. New TAD boundaries formed in ATRX KO show reduced insulation scores indicative of less frequent contacts between neighboring TADs and increased boundary strength (Figures 51 and 52). As anticipated, TADs that form in ATRX KO have significantly lower insulation scores compared to the same genomic coordinates in WT (Figure 53, bottom).

CTCF is essential for maintaining TAD organization (Nora et al., 2017). We re-examined our CUT&RUN data of CTCF peaks classified by whether they fell within TAD boundaries that were shared between WT and ATRX KO, lost from WT, or gained in ATRX KO. We found that CTCF peaks within ATRX KO-specific TAD boundaries had significantly larger increases in binding in ATRX KO mESCs compared to non-TAD boundary CTCF peaks or CTCF peaks in shared and WT-specific boundaries (Figure 54).

We next examined the enrichment of significantly gained and lost CTCF sites (Figure 5) for TAD boundaries. Both gained and lost sites were under-enriched in shared TAD boundaries. Notably, lost CTCF sites were enriched in WT-specific TAD boundaries (1.59-fold enrichment, $p = 4.32 \times 10\text{-}8$) while gained CTCF sites were underrepresented

(1.23-fold underenrichment, p = 0.04). Conversely, gained CTCF sites were enriched in KO-specific TAD boundaries (1.38-fold enrichment, p = 6.46 x 10-6) while lost sites were depleted (1.18-fold underenrichment, p = 0.027). Thus, redistribution of CTCF binding upon ATRX loss may weaken key TAD boundaries and induce the collapse of largerscale domain architecture into smaller domains demarcated by de novo CTCFoccupied boundaries. Chromatin loops also increased in number in ATRX KO cells and to a much greater extent than was observed with TADs (13,349 in ATRXKO compared to 8,548 in WT; Figure 55). As with TADs, we found that some larger chromatin loops called in WT appeared to be lost in ATRX KO, while many smaller loops were gained in

ATRX KO (Figure 56, left) resulting in an overall decrease in loop size (Figure 56, right). We defined sets of 2,271 “WT-specific” loops and 7,062 “ATRX KO-specific” loops based on overlap of loop anchors, calling a loop as specific to WT if either anchor was not shared in ATRX KO and vice versa. Aggregate loop analysis revealed that WTspecific loops were weakened upon ATRX loss, although some moderate level of interaction was retained (Figure 57, top). In contrast, 7,062 “ATRXKO-specific” loops were characterized by strong gain of interactions over regions with weak interactions in WT mESCs (Figure 57, bottom). Chromatin loops can facilitate enhancer-promoter interactions to promote gene expression (Rao et al., 2014). We performed RNA-Seq on WT and ATRXKO mESCs, then defined sets of genes that fall within shared, WTspecific, or ATRXKO-specific loops (Sup. Table 1) and examined their expression. Our analysis showed that genes falling within ATRX KO-specific loops trended strongly towards upregulation in ATRX KO mESCs, while genes in WT-specific loops were decreased slightly overall and genes in shared loops were centered around zero change (Figure 58). Overall, our data indicate that ATRX regulates genome organization at several scales, and that ATRX deficiency induces widespread rewiring of TADs and chromatin loops that can deregulate gene expression.

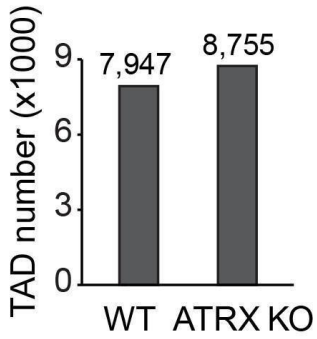

Fig. 46 Bar chart showing number of identified TADs in wildtype and ATRX KO mESCs.

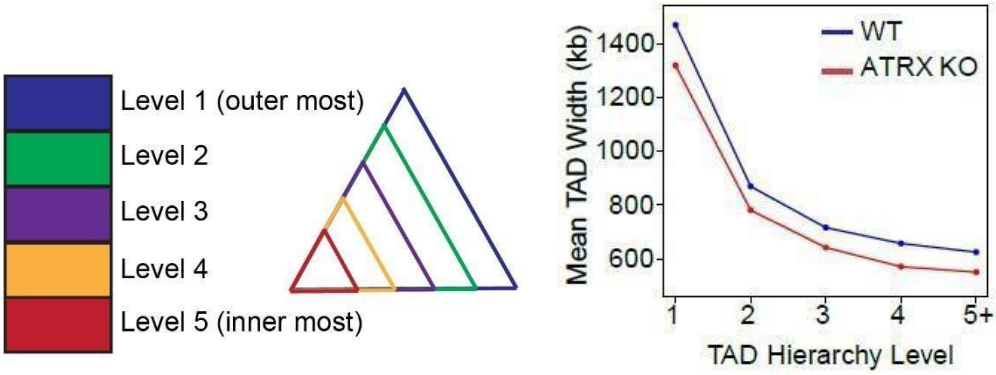

Fig. 47 Left, schematic of OnTAD level definitions. Right, lineplot of mean TAD widths for each hierarchal TAD level in WT and ATRX KO mESCs. (Work in progress)

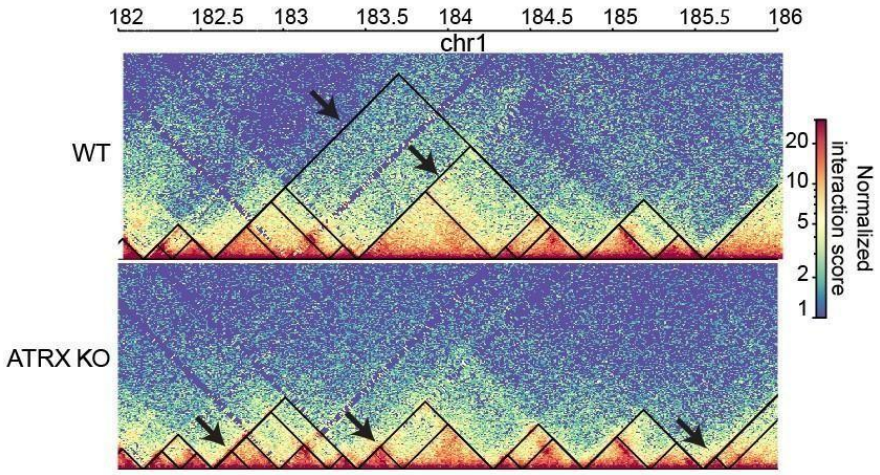

Fig. 48 10-kb resolution Hi-C maps of a region in chromosome 1 showing normalized interaction scores in wildtype (top) and ATRX KO (bottom) mESCs. Black borders denote identified TADs. Black arrows in top panel indicate TADs identified in WT that are lost in ATRX KO, while black arrows in bottom panel indicate TADs absent in WT that are gained in ATRX KO.

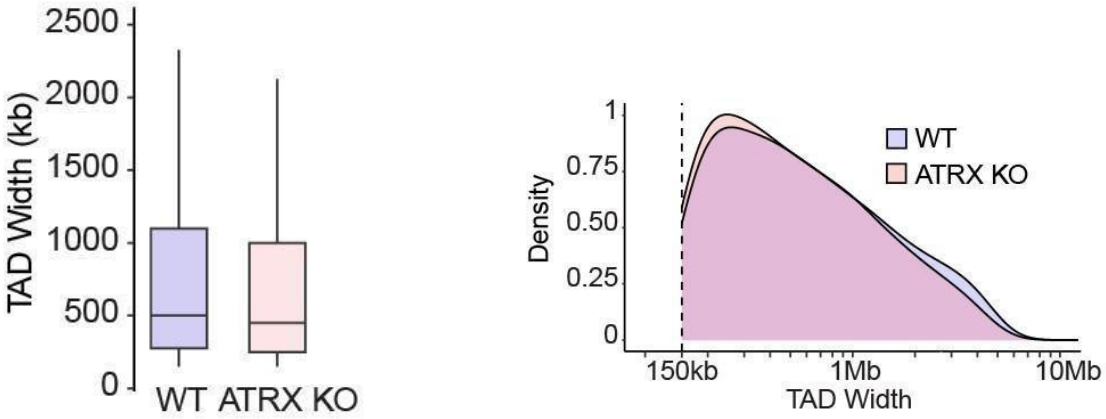

Fig. 49 Boxplot of TAD widths in wildtype and ATRX KO mESCs. Box, 25th percentile – median – 75th percentile. Whiskers extend to 1.5x interquartile range. **Fig. 50** Density plot of TAD widths in wildtype and ATRX KO mESCs. Dotted line denotes minimum TAD size of 150kb.

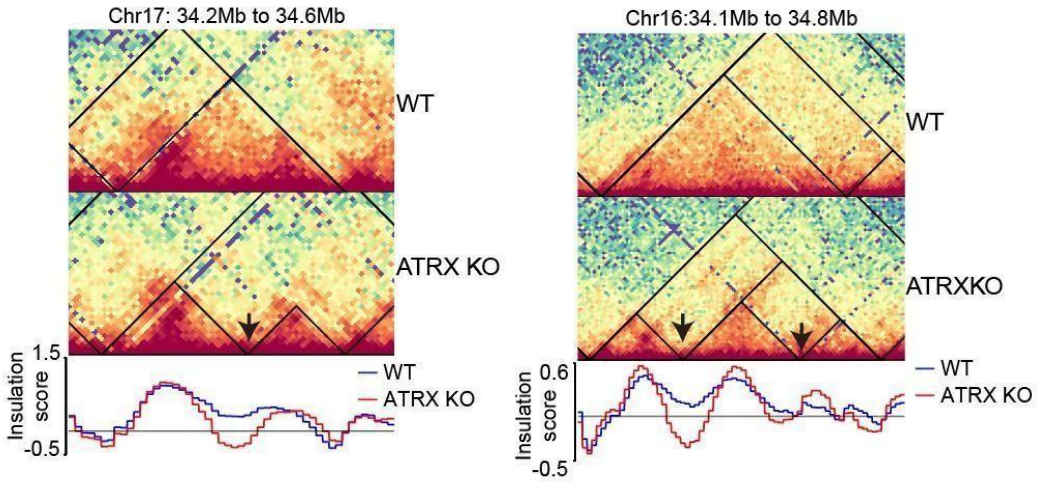

Fig. 51 Top, 10-kb resolution Hi-C maps of a region in chromosome 17 showing normalized interaction scores in wildtype (top) and ATRX KO (bottom) mESCs. Black borders denote identified TADs. Black arrow in bottom Hi-C map indicates a TAD boundary absent in WT that is gained in ATRX KO, forming two new and ATRX KO-specific TADs. Bottom, insulation score of 10-kb windows in WT and ATRX KO mESCs. **Fig. 52** Top, 10-kb resolution Hi-C maps of a region in chromosome 16 showing normalized interaction scores in wildtype (top) and ATRX KO (bottom) mESCs. Black borders denote identified TADs. Black arrows in bottom Hi-C map indicate TAD boundaries absent in WT that are gained in ATRX KO, forming new ATRX KO-specific TADs. Bottom, insulation score of 10-kb windows in WT and ATRX KO mESCs.

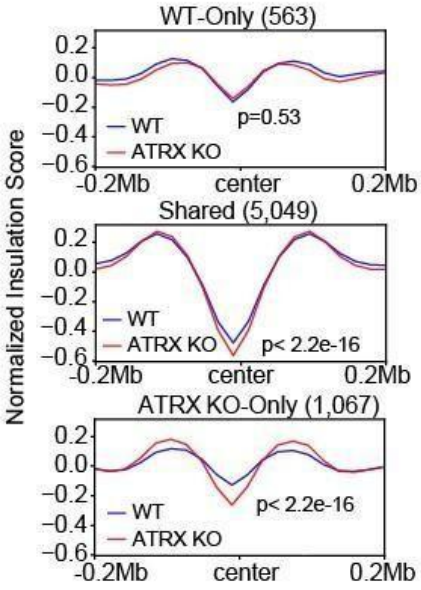

Fig. 53 Signal profile plots showing insulation score in wildtype and ATRX KO mESCs across TAD boundaries that are only identified as boundaries in WT (top), identified in both WT and ATRX KO (middle), or identified in ATRX KO alone (bottom).

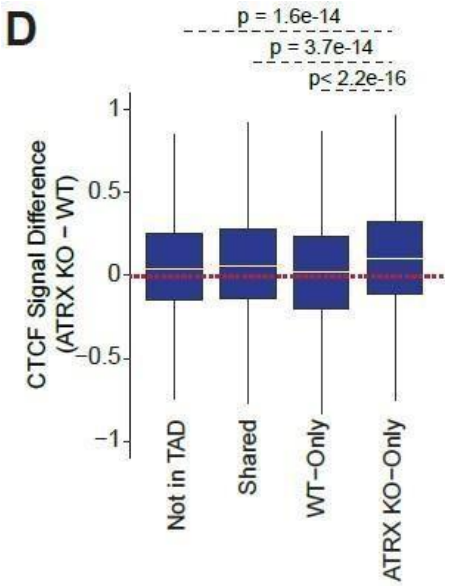

Fig. 54 Boxplot of log2 CTCF signal fold changes in ATRX KO versus wildtype mESCs of CTCF sites that are not at TAD boundaries, fall within shared TAD boundaries called in both WT and ATRX KO, or fall within TAD boundaries called only in WT or ATRX KO. Box, 25th percentile – median – 75th percentile. Whiskers extend to 1.5x interquartile range.

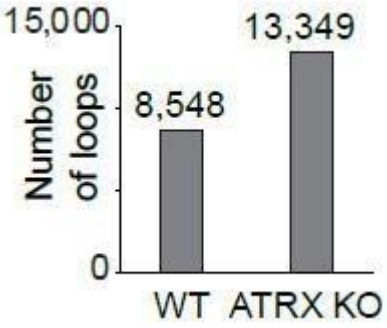

Fig. 55 Bar chart showing number of called chromatin loops in wildtype and ATRX KO mESCs.

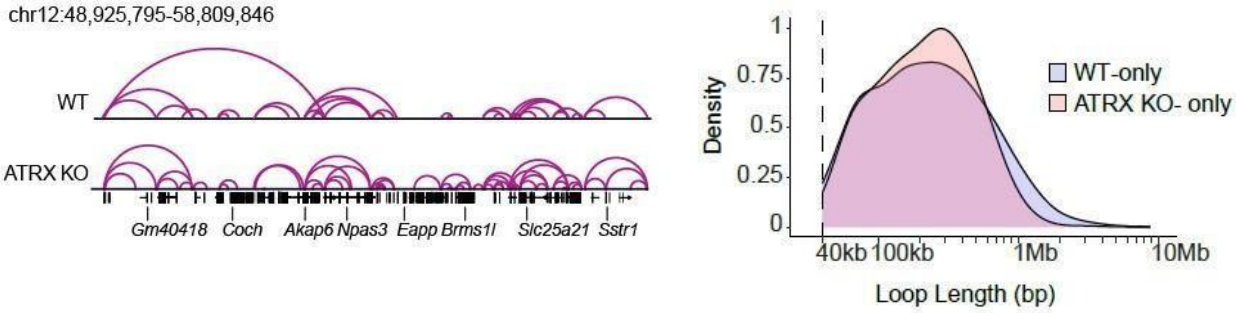

Fig. 56 On the left, Genome browser view of a region in chromosome 12 showing called chromatin loops in wildtype and ATRX KO mESCs. Select genes are labeled below loop tracks. On the right, Density plot of chromatin loop sizes in WT and ATRX KO mESCs. Dotted line denotes minimum loop size of 40kb.

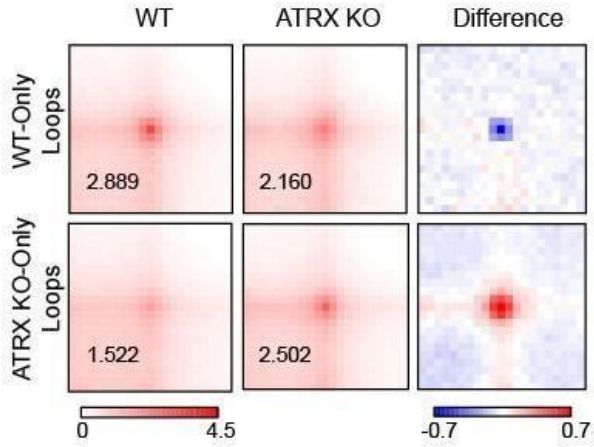

Fig. 57 Normalized aggregate peak analysis (APA) of 10-kb resolution HiC data comparing chromatin loop strength in wildtype and ATRX KO mESCs across WT-specific loops (top) or ATRX KO-specific loops (bottom). A loop was defined as WT-only if either anchor was not identified in a loop called in ATRX KO, and vice versa. Peak to lower left (P2LL) ratios are indicated in the lower left corners of APA plots. Rightmost plots display the difference in scores between WT and ATRX KO mESCs.

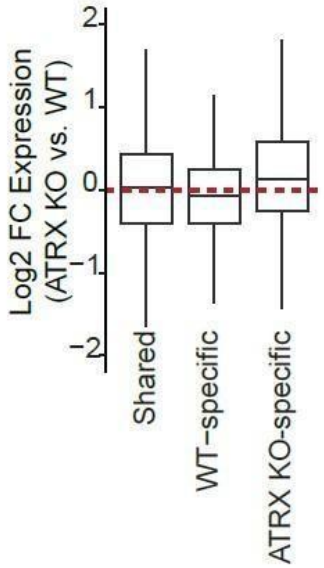

Fig 58 Boxplot of fold change expression in ATRX KO compared to WT of genes falling within shared, WTspecific, or ATRX KO-specific loops.

LTR derepression and TAD reorganization in ATRX KO contribute to gene upregulation

ATRX promotes silencing of various types of transposable elements (TEs) in part by reducing their chromatin accessibility (Sadic et al., 2015b). We analyzed our RNA-seq data to identify differentially expressed TEs and found a deregulation of several ERVK, ERVL, ERV1 and Long interspersed nuclear element 1 (LINE 1) subfamilies that were skewed toward derepression (Figure 59). Given the large number of LTR subfamilies identified by this analysis, we focused on finding individual LTR genomic loci that undergo expression changes upon ATRX loss. We identified 2,163 differentially expressed LTRs, of which 1,432 (66.2%) were upregulated in ATRX KO and 731 (33.8%) were downregulated. The distribution of upregulated versus downregulated elements varied by LTR type. For example, 84% of differentially expressed ERVL were upregulated (Figure 60), compared to 61% of ERVK and 71% of ERV1 elements (Figures 61 and 62).

LTRs can play critical roles in gene regulation by acting as promoters or enhancers (Gifford et al., 2013; Wong et al., 2025). For example, ERV1 retrotransposons, which we identified as largely upregulated in ATRX KO (Figure 62), are highly enriched for OCT4 binding in mESCs (Kunarso et al., 2010). Loss of factors that mediate repression of TEs, such as LSD1/KDM1A, was shown to result in deregulation not only of TEs themselves, but also of genes that are proximal to TEs (Kunarso et al., 2010). Thus, we reasoned that derepression of LTRs in ATRX KO might similarly result in upregulation of nearby genes. To examine this possibility, we first identified genes that have direct genomic overlap with expressed LTRs, then asked whether these genes undergo expression changes upon ATRX loss and the correlation with overlapping LTRs. We found a strong correlation

between the expression change of a gene and expression change of the overlapping LTR (Figure 63) indicating that they are affected in tandem by ATRX loss.

Upregulation of LTRs that overlap gene bodies might alter gene expression by directly affecting the chromatin environment. Alternatively, these LTRs can also function as enhancers or alternate promoters to regulate expression of nearby genes (Thompson et al., 2016; Wong et al., 2025). Thus, we next examined whether genes upregulated upon ATRX loss are near upregulated LTRs. Differential expression analysis of WT and ATRX KO RNA-seq identified 3,593 genes that are significantly upregulated in ATRX KO and 3,552 genes that are downregulated (Figure 64). Interestingly, when looking at the distribution of differentially expressed genes across the genome, we found that upregulated but not downregulated genes tend to form clusters around upregulated LTRs, even without direct overlap (Figure 65). We measured the distance of upregulated, downregulated, and invariant genes to the closest upregulated LTR and found that upregulated genes were significantly closer to upregulated LTRs compared to invariant and downregulated genes, with a median distance of 765Kb compared to 1Mb for invariant and 1.19Mb for downregulated genes (Figures 66 and 67). When looking at a cumulative distribution of distance, we find that 39.6% of upregulated genes are within 500kb of an upregulated LTR, compared to only 31.2% of invariant genes and 25.7% of downregulated genes (Figure 68).

ATRX loss results in partitioning of larger TADs into smaller ones (Figure 48-50). We asked how frequently upregulated LTRs were in the same TAD as an upregulated gene in ATRX KO. Of 8,755 TADs called in ATRX KO mESCs, 4,846 contain an upregulated gene and 1,388 contain an upregulated LTR. Notably, 1,027 of the 1,388 TADs that contain an upregulated LTRs also contain an upregulated gene, representing a 1.34-fold enrichment ($p = 8.8 \times 10\text{-}55$). In contrast, downregulated genes were not in the same TADs as upregulated LTRs more than expected (1.01-fold enrichment, $p = 0.44$). On an LTR level, 59% of upregulated LTRs are in TADs that contain upregulated genes, compared to 23% of downregulated LTRs. This raises the possibility that the reorganization of TADs upon ATRX loss may place LTRs in contact with non-cognate genes, resulting in de novo LTR-gene loop formation and gene upregulation. We examined newly formed TADs as well as

shifted TAD boundaries to identify examples where upregulated LTRs were brought into closer proximity to genes with which they do not normally interact.

New TAD boundaries are formed in ATRX KO which result in an upregulated LTR at the 3' end of the Slc4a4 gene being brought closer to the Slc4a4 promoter (Figures 69, left and 70, top) and an upregulation of the gene in ATRX KO (Figure 71, left). In another example, shifting of a TAD boundary normally within the M1ap gene in WT cells to an upstream location results in de novo loop formation between an upregulated LTR in the Slc4a5 gene and the Sema4f promoter (Figures 69 right and 70 bottom) that also brings the upregulated LTR closer to the promoter of M1ap. Accordingly, both Sema4f and M1ap are upregulated in ATRX KO (Figures 71 center and right). Our findings point to a model where changes in genome architecture upon ATRX loss can contribute to gene dysregulation through LTR co-option (2ndmodel).

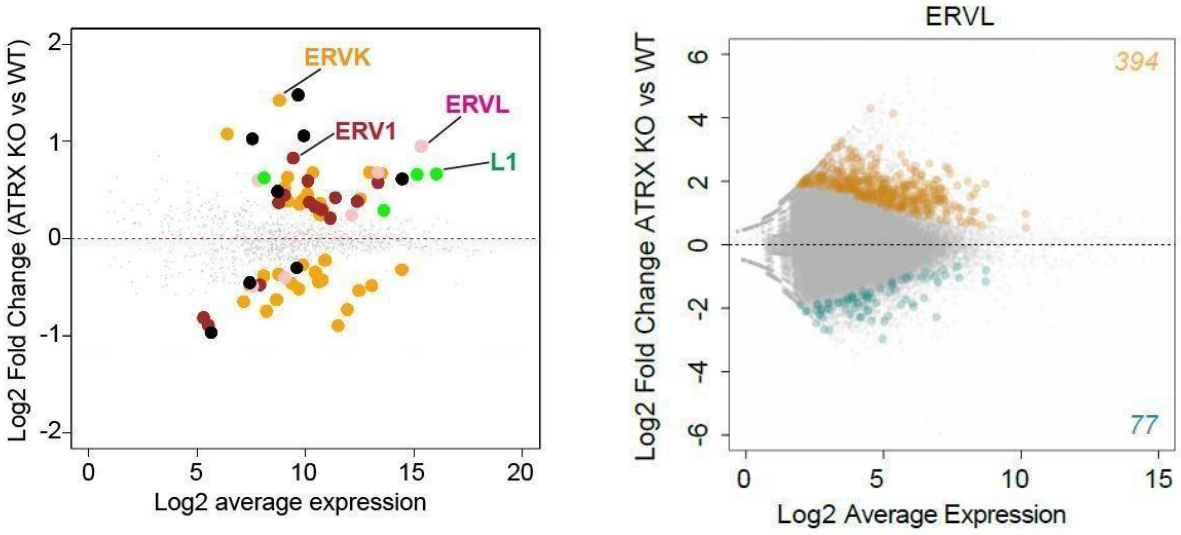

Fig. 59 MA plot of subfamily-level transposable element expression between wildtype and ATRX KO mESCs. Colored dots indicate significantly upregulated or downregulated TE subfamilies of various classes.
Fig. 60 MA plot of transposable element expression (individual loci) between wildtype and ATRX KO

mESCs. Red dots indicate significantly upregulated ERVL long terminal repeat (LTR) elements, while blue dots indicate significantly downregulated ERVL loci.

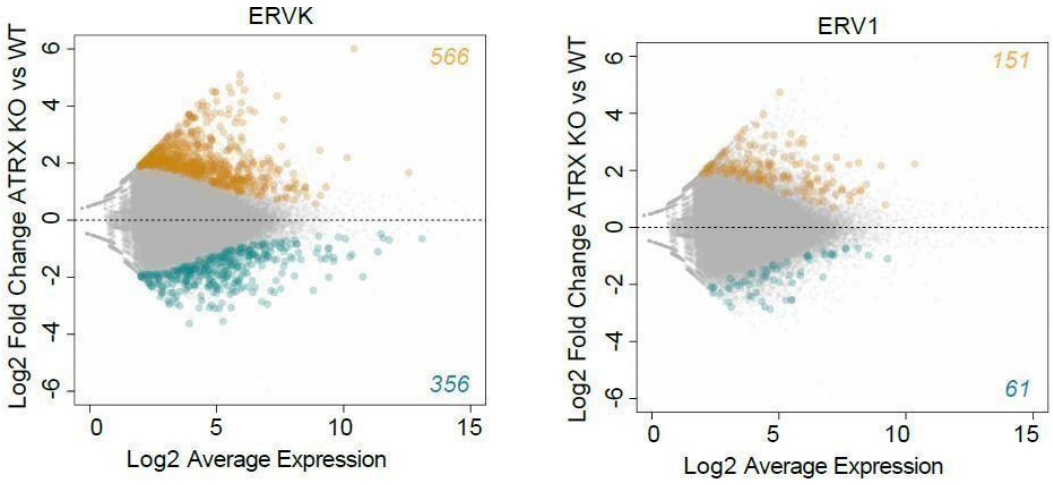

Fig. 61 MA plot of transposable element expression (individual loci) between wildtype and ATRX KO mESCs. Red dots indicate significantly upregulated ERVK long terminal repeat (LTR) elements, while blue dots indicate significantly downregulated ERVK loci. **Fig. 62** MA plot of transposable element expression (individual loci) between wildtype and ATRX KO mESCs. Red dots indicate significantly upregulated ERVK long terminal repeat (LTR) elements, while blue dots indicate significantly downregulated ERVK loci.

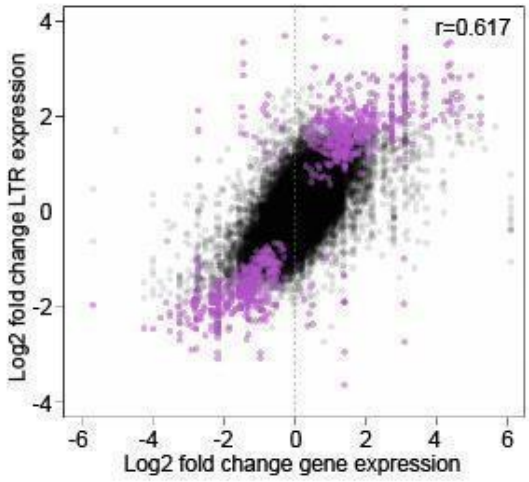

Fig. 63 Scatterplot showing correlation of gene expression and LTR expression between wildtype and ATRX KO mESCs. Each dot represents an LTR-gene pair by genomic overlap and shows the log2 fold change in expression (ATRX KO vs. WT) of the gene versus the log2 expression fold change of the overlapping LTR. Violet dots indicate LTR-gene pairs where the LTR overlapping the gene is significantly differentially expressed (adjusted p-value < 0.05).

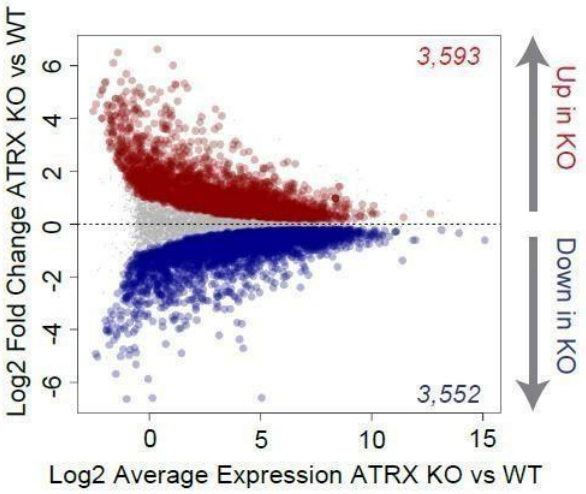

Fig. 64 MA plot of gene expression between wildtype and ATRX KO mESCs. Red dots indicate 3,593 significantly upregulated genes, while blue dots indicate 3,552 significantly downregulated genes (adjusted p-value <= 0.05).

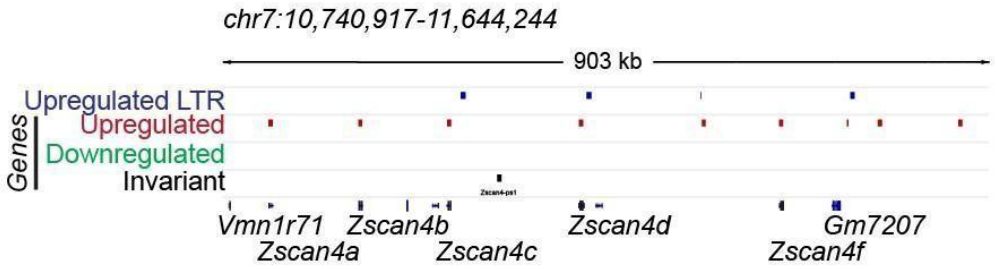

Fig. 65 Genome browser view of a region in chromosome 7 showing positions of significantly upregulated LTRs and significantly upregulated or invariant (not significantly DE) genes. No downregulated genes are present in the window.

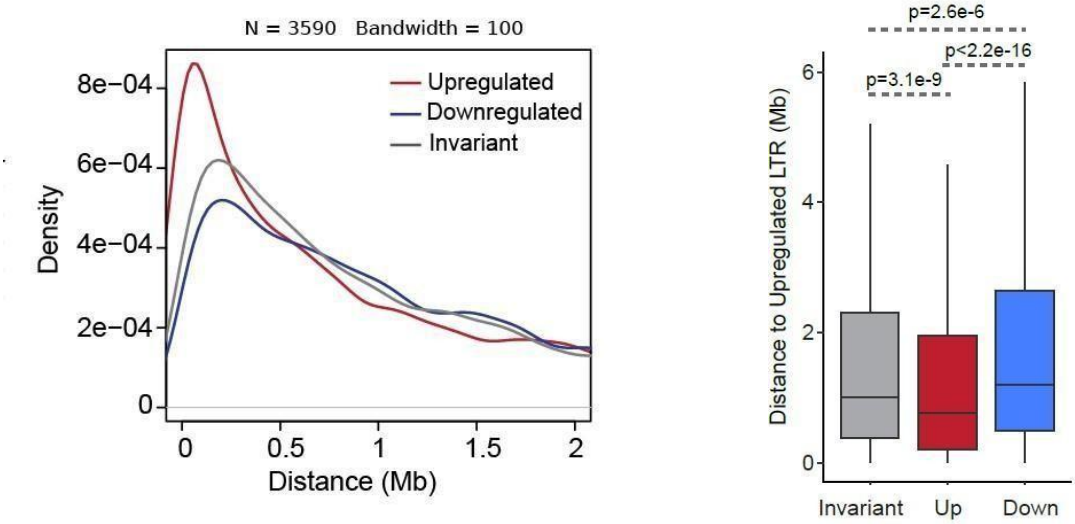

Fig 66 Density plot showing distance between upregulated, downregulated, or invariant genes and the nearest upregulated LTR. Arrows indicate the distance at which each density distribution is highest. **Fig 67** Boxplot of distance between invariant, upregulated, or downregulated genes to the nearest upregulated LTR element. p-values, Welch's two-sided t-test. Box, 25th percentile, median, and 75th percentile. Whiskers extend to 1.5x interquartile range; outliers not displayed.

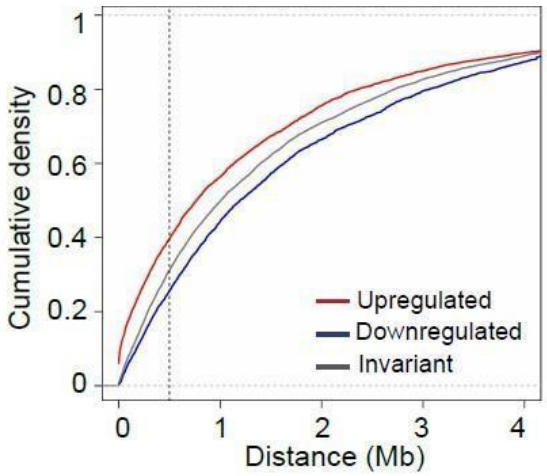

Fig. 68 Cumulative density plot of distance between upregulated, downregulated, or invariant genes and the nearest upregulated LTR. Dotted line indicates 500kb distance.

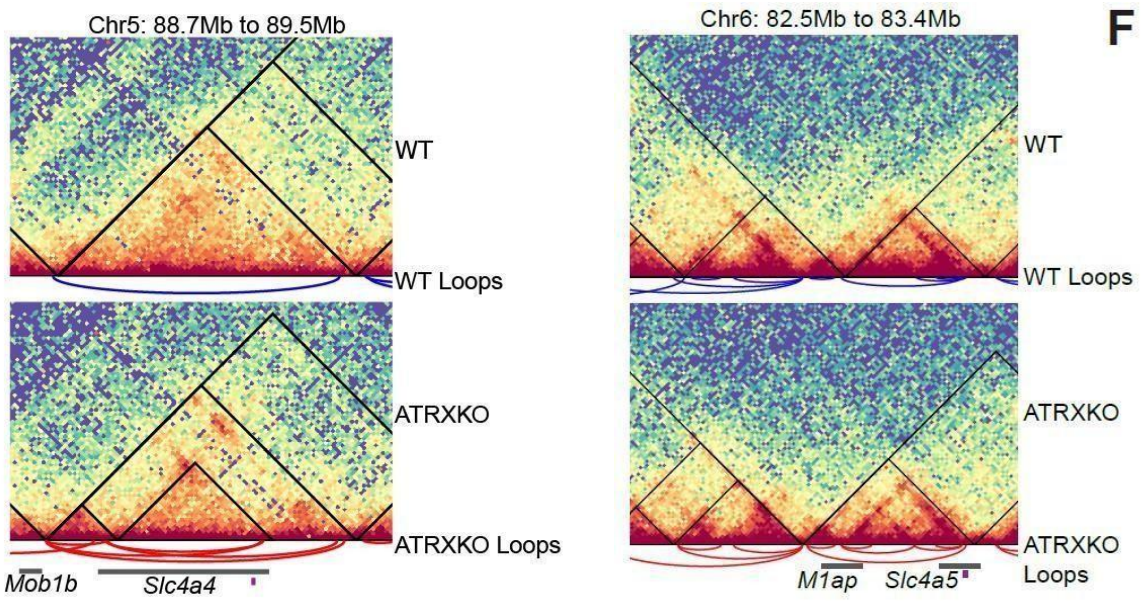

Fig 69 On the left, 10-kb resolution Hi-C maps of a region in chromosome 5 showing normalized interaction scores in wildtype (top) and ATRX KO (bottom) mESCs. Black borders denote identified TADs. Blue and red arcs indicate chromatin loops called in wildtype and ATRX KO mESCs, respectively. The locations of the upregulated Mob1b and Slc4a4 genes are labeled. Dark red box below the Slc4a4 gene indicates the location of an upregulated LTR. On the right, 10-kb resolution Hi-C maps of a region in chromosome 6 showing normalized interaction scores in WT (top) and ATRX KO (bottom) mESCs. Black borders denote identified TADs. Blue and red arcs indicate chromatin loops called in wildtype and ATRX KO mESCs, respectively. The locations of the upregulated M1ap and Slc4a5 genes are labeled. Dark red box below the Slc4a5 gene indicates the location of an upregulated LTR.

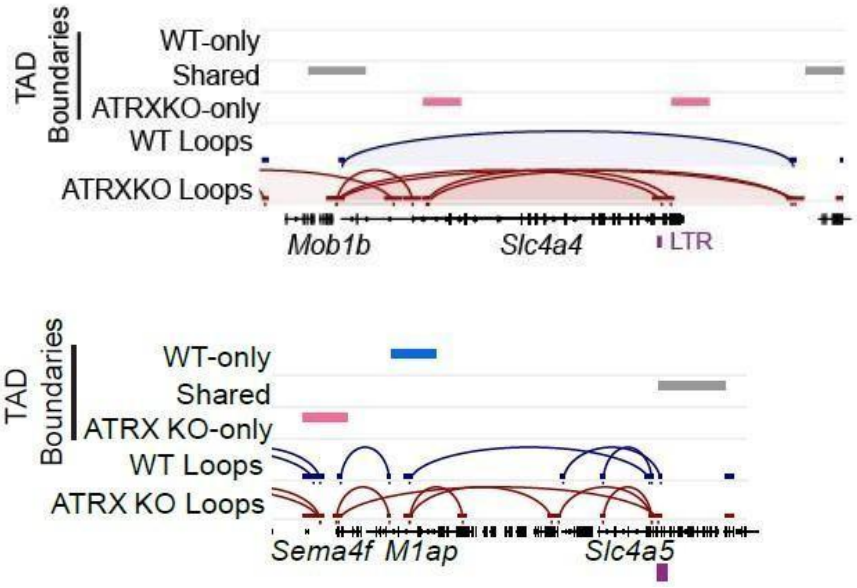

Fig 70 Top, genome browser view of the same region in panel G showing the location of TAD boundaries called in only one or both of wildtype and ATRX KO mESCS; loops called in wildtype and ATRX KO mESCs; and the locations of genes and an upregulated LTR. Bottom, genome browser view of the same region in panel G showing the location of TAD boundaries called in only one or both of WT and ATRX KO mESCs; loops called in WT and ATRX KO mESCs; and the locations of genes and upregulated LTR.

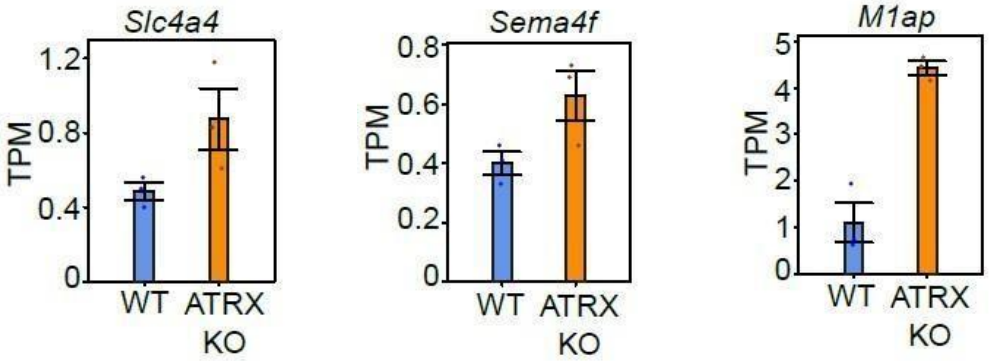

Fig 71 On the left, Bar plot of RNA-seq expression of Slc4a4 in transcripts per million (TPM) in WT and ATRX KO. Data are presented as mean values +/- SEM. Dots indicate 3 independent biological replicates. On the center and on the right, Bar plot of RNA-seq expression of Sema4f and M1ap in transcripts per million (TPM) in WT and ATRX KO. Data are presented as mean values +/- SEM. Dots indicate 3 independent biological replicates.

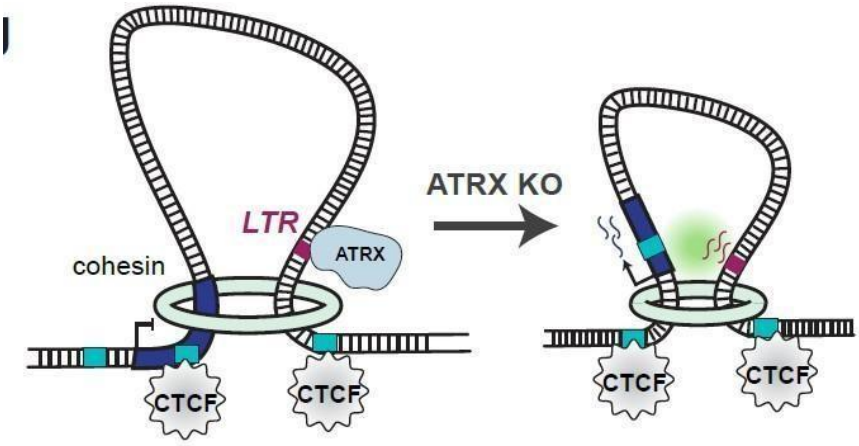

2nd Model for ATRX-mediated deregulation of gene expression. Left – ATRX mediates TAD and loop formation through its regulation of CTCF localization, in addition to silencing expression of LTR elements. Right – in the absence of ATRX, reorganization of TADs and loops places gene promoters in transcriptionally active neighborhoods and in proximity to derepressed LTRs that may act as enhancers to promote aberrant gene expression.

Materials and Methods

Cell lines and cell culture

E14 mouse embryonic stem cells (mESCs) were cultured on 0.1% gelatin-coated plates in media containing DMEM, 15% fetal bovine serum (Gibco), 1x MEM non-essential amino acids (Gibco 11140), 1x GlutaMAX (Gibco 35050), 25mM HEPES, 100U/ml PenStrep, 55μM 2-mercaptoethanol, and LIF (Sigma, ESGRO).

Generation of knockout and knockdown cell lines

HIRA knockout cell line was generated by transfecting PX459-HIRA-KO sgRNA plasmid (Addgene plasmid #186938) into mESCs. HIRA KO clones were selected with puromycin

and screened by Western blot. ATRX KO mESC cell line was described previously(Bieluszewska et al. 2022). DAXX KO cell line was generated by transfecting PX459-DAXX-KO sgRNA plasmid (Supplementary Table 2) into mESCs, selecting with puromycin and screening by western blot. Stable H3.3 knockdown cell lines were generated by transfecting mESCs with a mix of two plasmids containing shRNAs targeting H3.3 (Supplementary Table 2). Clones were selected with puromycin and H3.3 knockdown was validated by western blot on acid extracted histones.

Transient knockdown of ATRX

E14 cells were seeded at 1 x 105 cells/well in a 6-well plate and transfected with pLKO.1 shRNA-ATRX using Lipofectamine 3000 following the manufacturer's protocol. Scrambled shRNA was used as a negative control. Cells were collected 72hr posttransfection for Western blot, CUT&RUN, and ERRBS.

CUT&RUN

CUT&RUN was performed as previously described(Skene and Henikoff 2017; Skene et al. 2018) using CTCF antibody (Cell Signaling 3418S), H3.3 antibody (EpiCypher, 130061), or HIRA antibody (ActiveMotif 39457). Briefly, 500,000 to 5 million cells were washed two times in wash buffer (20 mM HEPES pH 7.5, 0.15 M NaCl, 0.5 mM spermidine, 1x Roche cOmplete protease inhibitor), then resuspended in wash buffer and immobilized onto BioMag Plus Concanavalin A beads for 1 hour at room temperature with rotation. Cells were resuspended in 50µL antibody buffer (wash buffer containing 0.02% digitonin and 2mM EDTA). 5µg CTCF antibody, 0.5µg H3.3 antibody, or 5µg HIRA antibody was added and samples were rotated overnight at 4°C. Cells were washed once with digitonin-wash buffer (wash buffer containing 0.02% digitonin) and resuspended in 50µL digitonin-wash buffer. Protein A-MNase was added to a final concentration of 700 ng/ml and samples were incubated at 4 °C with rotation for 1 h. Cells were washed twice with digitonin-wash buffer and resuspended in 100 µL digitonin-wash buffer. For MNase activation, CaCl2 was added to a final concentration of 2 mM and beads were incubated in wet ice at 0 °C for 30 min. 100 µL 2x STOP buffer (340 mM NaCl, 20 mM EDTA, 4 mM EGTA, 0.02% Digitonin, 5 µg RNase A, 50 µg/ml linear acrylamide)

containing heterologous Drosophila spike-in DNA was added to halt the MNase reaction. Cells were incubated at 37 °C for 10 min to release cleaved DNA fragments, centrifuged at 4 °C at 16,000 × g for 5 min, and supernatants transferred to new tubes. 2 µL 10% SDS and 5 µg proteinase K were added and samples were incubated at 70 °C for 10 min. DNA was purified with phenol:chloroform:isoamyl alcohol (PCI) extraction and ethanol precipitation.

RNA-Seq

RNA was extracted from mESCs using Trizol (Invitrogen) and subjected to Turbo DNase digestion (Ambion AM2238). RNA was rRNA-depleted using FastSelect -rRNA HMR (Qiagen) and converted to cDNA using Ultra II Directional RNA Library Prep Kit (NEB E7760).

CUT&RUN and RNA-Seq library preparation and sequencing

DNA (CUT&RUN) and cDNA (RNA-Seq) samples were end-repaired using End-Repair Mix (Enzymatics), followed by A-tailing with Klenow Fragment (3′→5′ exo−) (Enzymatics).

Samples were purified using MinElute columns (Qiagen) and Illumina adapters (NEB #E7600) were ligated using Rapid T4 DNA Ligase (Enzymatics). Libraries were sizeselected to remove adapter dimers using AMPure XP beads (Beckman Coulter). Library amplification was carried out using dual-index primers (NEB #E7600) and Q5 HighFidelity DNA Polymerase (NEB #M0491). Amplified libraries were purified with AMPure XP and sequenced on Illumina NextSeq 1000 using 2 × 61 bp paired-end reads.

Enhanced reduced representation bisulfite sequencing (ERRBS)

5 x 106 cells per replicate were harvested and washed in 1x PBS. Genomic DNA was extracted by suspending cell pellets in TE buffer containing SDS and proteinase K, incubating overnight at 55°C, and extracting with PCI followed by ethanol precipitation.

1 µg of high-quality genomic DNA was mixed with 10pg of unmethylated lambda phage DNA as a conversion control, then digested with 10 µL of MspI (New England Biolabs, NEB #R0106T) in rCutSmart buffer overnight at 37°C. Following digestion, the reaction

was purified using a PCR Purification Kit (Qiagen #28006) and DNA eluted in 15μL of EB. Digested genomic DNA was end-repaired using End-Repair Mix, A-tailed with Klenow Fragment (3′→5′ exo−), and purified using MinElute columns. Methylated adapters (NEB #E7536) were ligated with Rapid T4 DNA Ligase. Following adapter ligation, ERRBS samples were treated with 1μL of Uracil-DNA Glycosylase (Enzymatics) at 37°C for 15 min. Libraries then underwent right-tailed size selection using AMPure XP beads to recover fragments below 400bp in size. Bisulfite conversion was performed on sizeselected libraries using the EZ DNA Methylation-Gold Kit (Zymo Research #D5005), following the manufacturer's protocol. Library amplification was carried out using dualindex primers and Q5U DNA Polymerase (NEB #M0515S). Amplified libraries were purified with AMPure XP and sequenced on Illumina NextSeq 1000 using 2 × 61 bp pairedend reads.

Hi-C

Hi-C was performed using the Arima Genomics Hi-C+ for High-Coverage Kit on 4 x 106 million cells per sample and library preparation with the NEBNext Ultra II DNA Library Prep Kit for Illumina (NEB #E7645). Amplified Hi-C libraries were sequenced on Illumina NextSeq 1000 using 2 × 61 bp paired-end reads.

Repli-Seq

Repli-Seq to assay replication timing of wildtype and ATRX KO mESCs was performed as previously described(Marchal et al. 2018). Briefly, 1 x 107 BrdU-treated cells per condition were FACS sorted resulting in collection of roughly 480,000 cells for each early and late fraction. Cells were split into 4x aliquots and one aliquot per early/late fraction and condition, corresponding to 120,000 cells, was used for DNA extraction. Extracted DNA was further divided into 6 aliquots, with each aliquot representing one replicate and corresponding to 20,000 cells. DNA aliquots were sonicated on a Covaris ME220 instrument using the settings 70 W peak power, 20% duty cycle, 200 cycles/burst for 120 s at 4 °C. Libraries were prepared from sonicated DNA using the NEBNext Ultra II DNA Library Prep Kit, subjected to BrdU IP followed by PCR amplification, and sequenced on Illumina NextSeq 1000 using 2 × 61 bp paired-end reads.

Reads from RepliSeq early and late fraction samples were processed as described previously(Marchal et al. 2018). Briefly, reads were aligned to the mm10 genome with Bowtie2 version 2.2.9(Langmead and Salzberg 2012) and PCR read duplicates were removed from aligned BAM files using Samtools(Li et al. 2009). Read coverage was quantified across 50-kb non-overlapping windows tiled across the genome. Replication timing for each window was measured by taking the log2 ratio of coverage between early and late fractions ("E/L ratio"), with an E/L ratio greater than 0 representing a higher proportion of early fraction-originating reads and vice versa. E/L ratios were Loess smoothed to reduce noise. Quantile normalization of E/L ratios was not performed to avoid masking of global changes in replication timing.

CUT&RUN sequencing data processing and analysis

CUT&RUN reads were mapped to the mm10 mouse genome using Bowtie2 with default paired-end settings. RPM normalized BigWig tracks were generated using bamCoverage function in deepTools version 3.5.1(Ramírez et al. 2016) using the parameters "--binSize 5 --extendReads --normalizeUsing CPM --blackListFileName", which removes a known set of ENCODE blacklist regions(Amemiya et al. 2019). Signal plots and heatmaps were generated with deepTools and the multiBigwigSummary function in deepTools was used to calculate average signal across regions for boxplots and scatterplots.

CUT&RUN peaks were called with MACS2 2.2.184(Zhang et al. 2008) using the parameters "-f BAMPE -g mm --keep-dup all". Differential binding analysis of CUT&RUN data was performed in R version 3.6.1 using DiffBind version 2.12.0(Rory Stark 2011). Peaks present in at least two samples and that were not in an unknown contig or blacklisted region were kept for analysis, and differential occupancy was called using the edgeR method and an FDR cutoff of 0.05. Genomic annotation of peaks was performed using ChIPseeker version 1.20.0(Yu et al. 2015). Motif analysis of peaks was performed using the MEME suite(Bailey et al. 2015). Overlap of CTCF peaks with LTR regions was determined using simple overlap with the GenomicRanges package in R against a list of LTRs from RepeatMasker(Smit et al. 2013-2015).

ERRBS alignment and data processing

ERRBS paired-end reads were first trimmed for adapter sequences and low-quality bases using Trim Galore (v0.6.10)(Martin 2011) with the "--rrbs" mode, which is specifically designed for MspI digestion patterns. Trimmed reads were aligned to an in silico bisulfiteconverted version of the mm10 reference genome using Bismark v0.24.1(Krueger and Andrews 2011) in paired-end mode, with Bowtie2 as the underlying aligner. Following alignment, methylation quantification was performed with the "bismark_methylation_extractor" function of Bismark using the "--ignore_r2 3" option to discard the first three bases from read 2, which are known to be biased due to MspI digestion, and the " --cytosine_report" option to generate single-base resolution methylation calls.

Cytosine methylation data were further processed and analyzed using the methylKit package version 1.24.0(Akalin et al. 2012) in R. To minimize technical noise, CpG sites with coverage below 10 reads or above the 99.9th percentile of coverage amongst all covered CpG sites were excluded using the filterByCoverage function. The filtered dataset was then normalized for read depth across samples using the median method implemented in normalizeCoverage. To assess regional methylation patterns, the percMethylation function was used to calculate mean methylation of covered CpGs over fixed, non-overlapping 1-kilobase windows across the genome, or over other regions of interest such as CTCF peaks.

RNA-seq alignment and analysis

RNA-Seq reads were aligned to mm10 using STAR version 2.7.9a(Dobin et al. 2013) and RSEM version 1.3.3(Li and Dewey 2011) was used to obtain estimated and TPM counts. Analysis of RNA-Seq data was performed in R using limma version 3.54.2(Ritchie et al. 2015) and edgeR version 3.40.2(Robinson et al. 2010) using an expression cutoff as determined using the built-in edgeR function "filterByExpr". Analysis of repeat element expression was performed using SQuIRE version 0.9.9.92(Yang et al. 2019) with default options. Briefly, a reference of repeat elements was built from RepeatMasker using the Build, Fetch, and Clean functions, and reads were aligned to the reference with the Map

function and quantified using the Count function. The Call function was used to identify differentially expressed repeat element subfamilies and loci.

Hi-C alignment and analysis

Hi-C reads were combined between two independent replicates, then aligned to the mm10 genome using Juicer(Durand et al. 2016) with default settings and an annotation file based on the Arima restriction enzyme digest. Hi-C contact maps were generated using FAN-C version 0.9.27(Kruse et al. 2020) and HiCExplorer version 3.7.6(Ramírez et al. 2018) from Knight-Ruiz normalized matrices. Eigenvector for A/B compartments was calculated using the “compartments” function in FAN-C. Differential compartment analysis was performed with dcHiC(Chakraborty et al. 2022) on 100kb resolution data. TADs were called with OnTAD version 1.4(An et al. 2019a), which identifies nested TADs and their hierarchal structure, using 25kb resolution data and default parameters. Insulation scores were computed using the “insulation” function in FAN-C. Chromatin loops were called using the HiCCUPS function in Juicer Tools on the CPU setting and default parameters.

Aggregate peak analysis (APA) matrices were generated using the APA function in Juicer

Tools. Subtraction maps of APA matrices were generated by subtracting WT from ATRX KO contact values for each individual pixel.

Discussion

Our data shows that prolonged and complete loss of ATRX in our model leads to widespread DNA demethylation (Fig. 8 and Fig. 9) and altered replication timing (Fig. 43). These changes are accompanied by profound disruptions in nuclear compartmentalization (Fig. 37, Fig. 38, and Fig. 39), including a shift from B to A compartments (Fig. 41), increased compartmental mixing (Fig. 40), and a marked loss of compartment integrity (Fig. 40). These findings are consistent with those of Du et al., who demonstrated that global DNA hypomethylation (achieved via DNMT1/DNMT3B double knockout) leads to replication timing heterogeneity, loss of allelic coordination, and weakened 3D genome compartmentalization. Their study highlights that DNA

methylation is essential not only for transcriptional repression but also for maintaining the precision of replication timing and the structural integrity of the genome (Du et al., 2021b).

Importantly, we did not observe any changes following a transient 72-hour ATRX knockdown (Fig. 11, Fig. 12, Fig. 13), suggesting that sustained ATRX deficiency is required to destabilize nuclear topology. Interestingly, the demethylation we observed aligns with clinical observations from Gibbons et al., who reported that patients with ATR-X syndrome exhibit abnormal DNA methylation patterns, particularly at repetitive sequences such as rDNA arrays, subtelomeric regions, and satellite repeats (Gibbons et al., 2000). Although ATRX expression in these patients is reduced rather than absent, their epigenetic phenotype mirrors our findings, raising the possibility that even partial (but prolonged) ATRX deficiency may predispose to conformational alterations in chromatin architecture.

Beyond its direct role in maintaining nuclear architecture, ATRX appears to exert an indirect regulatory influence on genome organization through CTCF. We observed a strong correlation between H3.3 and CTCF occupancy (Fig. 17 and Fig. 18), and found that disruption of the ATRX–DAXX–H3.3 complex affects genomic regions normally bound by CTCF (Fig. 21, Fig. 25, and Fig. 27), suggesting that ATRX mediated histone deposition may facilitate stable CTCF binding and boundary formation. This is particularly relevant in light of recent findings by Zhang et al., who showed that a single point mutation in CTCF (R567W, located in zinc finger 11) impairs its ability to maintain TAD boundaries, nuclear compartmentalization, and spatial gene regulation, leading to neurodevelopmental defects in both murine and cortical organoid models (Zhang et al., 2024). These findings underscore the importance of proper 3D genome organization in human brain development.

Interestingly, in ATRX-deficient cells, we observed a strong correlation between CTCF, HIRA, and H3.3 at loci enriched for LTR elements (Fig. 28, Fig. 31, Fig. 32, Fig. 33; Fig. 34, Fig. 35, Fig. 36), suggesting a compensatory mechanism. This observation prompted us to investigate the behavior of LTRs more closely.

In our ATRX knockout model, LTR elements were markedly upregulated (Fig. 59) and frequently repositioned into TADs (Fig. 69). These spatial rearrangements often placed LTRs in proximity to genes that were concurrently upregulated (Fig. 63, Fig. 65 - 68). These findings reveal a broader role for ATRX not only in repressing repetitive elements but also in preventing their physical integration into regulatory domains where they could influence nearby gene expression.

This mechanism aligns with the evolutionary trajectory of transposable elements, many of which (including LTRs) have acquired regulatory potential by embedding transcription factor binding sites and adopting enhancer or promoter like functions in a tissue-specific manner (Xie et al., 2013). Xie et al. also demonstrated that LTR enhancer activity is potentiated by DNA hypomethylation, a feature we observe in ATRX-deficient cells. Thus, ATRX loss may promote aberrant enhancer like behavior of LTRs through epigenetic deregulation, contributing to transcriptional rewiring.

A compelling future direction will be to investigate whether specific LTR- enhancer elements regulated by ATRX are functionally required during neurodevelopment. CRISPR-based perturbation of these LTRs could help determine their regulatory impact and clarify whether their activation contributes to lineage-specific transcriptional programs. Given that many transposable elements are developmentally regulated, it is plausible that these LTRs are normally silenced during specific windows of differentiation, and that ATRX plays a role in enforcing this temporal repression. It will also be important to examine chromatin architecture in patients derived ATR-X syndrome and ALT-positive tumor lines, to assess whether ATRX dependent structural features are conserved across developmental and disease contexts.

References

Aguilera, P., López-Contreras, A.J., 2023. ATRX, a guardian of chromatin. Trends Genet. 39, 505–519. https://doi.org/10.1016/j.tig.2023.02.009

An, L., Yang, T., Yang, J., Nuebler, J., Xiang, G., Hardison, R.C., Li, Q., Zhang, Y., 2019. OnTAD: hierarchical domain structure reveals the divergence of activity among TADs and boundaries. Genome Biol. 20, 282. https://doi.org/10.1186/s130590191893-y

Argentaro, A., Yang, J.-C., Chapman, L., Kowalczyk, M.S., Gibbons, R.J., Higgs, D.R., Neuhaus, D., Rhodes, D., 2007. Structural consequences of disease-causing mutations in the ATRX-DNMT3-DNMT3L (ADD) domain of the chromatinassociated protein ATRX. Proc. Natl. Acad. Sci. U. S. A. 104, 11939–11944. https://doi.org/10.1073/pnas.0704057104

Babikir, H., Wang, L., Shamardani, K., Catalan, F., Sudhir, S., Aghi, M.K., Raleigh, D.R., Phillips, J.J., Diaz, A.A., 2021. ATRX regulates glial identity and the tumor microenvironment in IDH-mutant glioma. Genome Biol. 22, 311. https://doi.org/10.1186/s13059-021-02535-4

Badens, C., Lacoste, C., Philip, N., Martini, N., Courrier, S., Giuliano, F., Verloes, A., Munnich, A., Leheup, B., Burglen, L., Odent, S., Van Esch, H., Levy, N., 2006. Mutations in PHD-like domain of the *ATRX* gene correlate with severe psychomotor impairment and severe urogenital abnormalities in patients with ATRX syndrome. Clin. Genet. 70, 57–62. https://doi.org/10.1111/j.13990004.2006.00641.x

Bonev, B., Cavalli, G., 2016. Organization and function of the 3D genome. Nat. Rev. Genet. 17, 661–678. https://doi.org/10.1038/nrg.2016.112

Bramswig, N.C., Caluseriu, O., Lüdecke, H.-J., Bolduc, F.V., Noel, N.C.L., Wieland, T., Surowy, H.M., Christen, H.-J., Engels, H., Strom, T.M., Wieczorek, D., 2017. Heterozygosity for ARID2 loss-of-function mutations in individuals with a Coffin–Siris syndrome-like phenotype. Hum. Genet. 136, 297–305. https://doi.org/10.1007/s00439-017-1757-z

Chatzinikolaou, G., Apostolou, Z., Aid-Pavlidis, T., Ioannidou, A., Karakasilioti, I., Papadopoulos, G.L., Aivaliotis, M., Tsekrekou, M., Strouboulis, J., Kosteas, T., Garinis, G.A., 2017. ERCC1-XPF cooperates with CTCF and cohesin to facilitate the developmental silencing of imprinted genes. Nat. Cell Biol. 19, 421–432. https://doi.org/10.1038/ncb3499

Chen, P., Wang, Y., Li, G., 2014. Dynamics of histone variant H3.3 and its coregulation with H2A.Z at enhancers and promoters. Nucl. Austin Tex 5, 21–27. https://doi.org/10.4161/nucl.28067

Choi, J., Kim, T., Cho, E.-J., 2024. HIRA vs. DAXX: the two axes shaping the histone H3.3 landscape. Exp. Mol. Med. 56, 251–263. https://doi.org/10.1038/s12276023-01145-3

Ciptasari, U., van Bokhoven, H., 2020. The phenomenal epigenome in neurodevelopmental disorders. Hum. Mol. Genet. 29, R42–R50.

https://doi.org/10.1093/hmg/ddaa175
Cukier, H.N., Lee, J.M., Ma, D., Young, J.I., Mayo, V., Butler, B.L., Ramsook, S.S., Rantus, J.A., Abrams, A.J., Whitehead, P.L., Wright, H.H., Abramson, R.K., Haines, J.L., Cuccaro, M.L., Pericak-Vance, M.A., Gilbert, J.R., 2012. The Expanding Role of MBD Genes in Autism: Identification of a *MECP2* Duplication and Novel Alterations in *MBD5* , *MBD6* , and *SETDB1* . Autism Res. 5, 385–397. https://doi.org/10.1002/aur.1251
Danussi, C., Bose, P., Parthasarathy, P.T., Silberman, P.C., Van Arnam, J.S., Vitucci, M., Tang, O.Y., Heguy, A., Wang, Y., Chan, T.A., Riggins, G.J., Sulman, E.P., Lang, F.F., Creighton, C.J., Deneen, B., Miller, C.R., Picketts, D.J., Kannan, K., Huse, J.T., 2018. Atrx inactivation drives disease-defining phenotypes in glioma cells of origin through global epigenomic remodeling. Nat. Commun. 9, 1057. https://doi.org/10.1038/s41467-018-03476-6
Delbarre, E., Ivanauskiene, K., Spirkoski, J., Shah, A., Vekterud, K., Moskaug, J.Ø., Bøe, S.O., Wong, L.H., Küntziger, T., Collas, P., 2017. PML protein organizes heterochromatin domains where it regulates histone H3.3 deposition by ATRX/DAXX. Genome Res. 27, 913–921. https://doi.org/10.1101/gr.215830.116
Dhayalan, A., Tamas, R., Bock, I., Tattermusch, A., Dimitrova, E., Kudithipudi, S., Ragozin, S., Jeltsch, A., 2011. The ATRX-ADD domain binds to H3 tail peptides and reads the combined methylation state of K4 and K9. Hum. Mol. Genet. 20, 2195–2203. https://doi.org/10.1093/hmg/ddr107
Diaz, A.A., 2022. Loss of ATRX suppresses anti-tumor immunity. Neuro-Oncol. 24, 901–902. https://doi.org/10.1093/neuonc/noac059
Drané, P., Ouararhni, K., Depaux, A., Shuaib, M., Hamiche, A., 2010. The deathassociated protein DAXX is a novel histone chaperone involved in the replicationindependent deposition of H3.3. Genes Dev. 24, 1253–1265. https://doi.org/10.1101/gad.566910
Du, Q., Smith, G.C., Luu, P.L., Ferguson, J.M., Armstrong, N.J., Caldon, C.E., Campbell, E.M., Nair, S.S., Zotenko, E., Gould, C.M., Buckley, M., Chia, K.-M., Portman, N., Lim, E., Kaczorowski, D., Chan, C.-L., Barton, K., Deveson, I.W., Smith, M.A., Powell, J.E., Skvortsova, K., Stirzaker, C., Achinger-Kawecka, J., Clark, S.J., 2021a. DNA methylation is required to maintain both DNA replication timing precision and 3D genome organization integrity. Cell Rep. 36, 109722. https://doi.org/10.1016/j.celrep.2021.109722
Du, Q., Smith, G.C., Luu, P.L., Ferguson, J.M., Armstrong, N.J., Caldon, C.E., Campbell, E.M., Nair, S.S., Zotenko, E., Gould, C.M., Buckley, M., Chia, K.-M., Portman, N., Lim, E., Kaczorowski, D., Chan, C.-L., Barton, K., Deveson, I.W., Smith, M.A., Powell, J.E., Skvortsova, K., Stirzaker, C., Achinger-Kawecka, J., Clark, S.J., 2021b. DNA methylation is required to maintain both DNA replication timing precision and 3D genome organization integrity. Cell Rep. 36, 109722. https://doi.org/10.1016/j.celrep.2021.109722
Duan, S., Nodelman, I.M., Zhou, H., Tsukiyama, T., Bowman, G.D., Zhang, Z., 2025. H3K56 acetylation regulates chromatin maturation following DNA replication. Nat.

Commun. 16, 134. https://doi.org/10.1038/s41467-024-55144-7 Dyer, M.A., Qadeer, Z.A., Valle-Garcia, D., Bernstein, E., 2017. ATRX and DAXX: Mechanisms and Mutations. Cold Spring Harb. Perspect. Med. 7, a026567. https://doi.org/10.1101/cshperspect.a026567

Elsässer, S.J., Noh, K.-M., Diaz, N., Allis, C.D., Banaszynski, L.A., 2015a. Histone H3.3 is required for endogenous retroviral element silencing in embryonic stem cells. Nature 522, 240–244. https://doi.org/10.1038/nature14345

Elsässer, S.J., Noh, K.-M., Diaz, N., Allis, C.D., Banaszynski, L.A., 2015b. Histone H3.3 is required for endogenous retroviral element silencing in embryonic stem cells. Nature 522, 240–244. https://doi.org/10.1038/nature14345

Ernst, C., 2016. Proliferation and Differentiation Deficits are a Major Convergence Point for Neurodevelopmental Disorders. Trends Neurosci. 39, 290–299. https://doi.org/10.1016/j.tins.2016.03.001

Eustermann, S., Yang, J.-C., Law, M.J., Amos, R., Chapman, L.M., Jelinska, C., Garrick, D., Clynes, D., Gibbons, R.J., Rhodes, D., Higgs, D.R., Neuhaus, D., 2011a. Combinatorial readout of histone H3 modifications specifies localization of ATRX to heterochromatin. Nat. Struct. Mol. Biol. 18, 777–782. https://doi.org/10.1038/nsmb.2070

Eustermann, S., Yang, J.-C., Law, M.J., Amos, R., Chapman, L.M., Jelinska, C., Garrick, D., Clynes, D., Gibbons, R.J., Rhodes, D., Higgs, D.R., Neuhaus, D., 2011b. Combinatorial readout of histone H3 modifications specifies localization of ATRX to heterochromatin. Nat. Struct. Mol. Biol. 18, 777–782. https://doi.org/10.1038/nsmb.2070

Fang, Y., Barrows, D., Dabas, Y., Carroll, T.S., Singer, S., Tap, W.D., Nacev, B.A., 2024. ATRX guards against aberrant differentiation in mesenchymal progenitor cells. Nucleic Acids Res. 52, 4950–4968. https://doi.org/10.1093/nar/gkae160

Garcia-Perez, J.L., Widmann, T.J., Adams, I.R., 2016. The impact of transposable elements on mammalian development. Dev. Camb. Engl. 143, 4101–4114. https://doi.org/10.1242/dev.132639

Garrick, D., Samara, V., McDowell, T.L., Smith, A.J.H., Dobbie, L., Higgs, D.R., Gibbons, R.J., 2004. A conserved truncated isoform of the ATR-X syndrome protein lacking the SWI/SNF-homology domain. Gene 326, 23–34. https://doi.org/10.1016/j.gene.2003.10.026

Ghirlando, R., Felsenfeld, G., 2016. CTCF: making the right connections. Genes Dev. 30, 881–891. https://doi.org/10.1101/gad.277863.116

Gibbons, R.J., McDowell, T.L., Raman, S., O'Rourke, D.M., Garrick, D., Ayyub, H., Higgs, D.R., 2000. Mutations in ATRX, encoding a SWI/SNF-like protein, cause diverse changes in the pattern of DNA methylation. Nat. Genet. 24, 368–371. https://doi.org/10.1038/74191

Gibbons, R.J., Picketts, D.J., Villard, L., Higgs, D.R., 1995. Mutations in a putative global transcriptional regulator cause X-linked mental retardation with αthalassemia (ATR-X syndrome). Cell 80, 837–845. https://doi.org/10.1016/00928674(95)90287-2

Gibbons, R.J., Wada, T., Fisher, C.A., Malik, N., Mitson, M.J., Steensma, D.P., Fryer, A., Goudie, D.R., Krantz, I.D., Traeger-Synodinos, J., 2008. Mutations in the chromatin-associated protein ATRX. Hum. Mutat. 29, 796–802. https://doi.org/10.1002/humu.20734

Gibbons, R.J., Wilkie, A.O., Weatherall, D.J., Higgs, D.R., 1991. A newly defined X linked mental retardation syndrome associated with alpha thalassaemia. J. Med. Genet. 28, 729–733. https://doi.org/10.1136/jmg.28.11.729

Gifford, W.D., Pfaff, S.L., Macfarlan, T.S., 2013. Transposable elements as genetic regulatory substrates in early development. Trends Cell Biol. 23, 218–226. https://doi.org/10.1016/j.tcb.2013.01.001

Goldberg, A.D., Banaszynski, L.A., Noh, K.-M., Lewis, P.W., Elsaesser, S.J., Stadler, S., Dewell, S., Law, M., Guo, X., Li, X., Wen, D., Chapgier, A., DeKelver, R.C., Miller, J.C., Lee, Y.-L., Boydston, E.A., Holmes, M.C., Gregory, P.D., Greally, J.M., Rafii, S., Yang, C., Scambler, P.J., Garrick, D., Gibbons, R.J., Higgs, D.R., Cristea, I.M., Urnov, F.D., Zheng, D., Allis, C.D., 2010. Distinct Factors Control Histone Variant H3.3 Localization at Specific Genomic Regions. Cell 140, 678–691. https://doi.org/10.1016/j.cell.2010.01.003

Groh, S., Schotta, G., 2017. Silencing of endogenous retroviruses by heterochromatin. Cell. Mol. Life Sci. CMLS 74, 2055–2065. https://doi.org/10.1007/s000180172454-8

Gulve, N., Su, C., Deng, Z., Soldan, S.S., Vladimirova, O., Wickramasinghe, J., Zheng, H., Kossenkov, A.V., Lieberman, P.M., 2022. DAXX-ATRX regulation of p53 chromatin binding and DNA damage response. Nat. Commun. 13, 5033. https://doi.org/10.1038/s41467-022-32680-8

Hafner, A., Park, M., Berger, S.E., Murphy, S.E., Nora, E.P., Boettiger, A.N., 2023. Loop stacking organizes genome folding from TADs to chromosomes. Mol. Cell 83, 1377-1392.e6. https://doi.org/10.1016/j.molcel.2023.04.008

He, Q., Kim, H., Huang, R., Lu, W., Tang, M., Shi, F., Yang, D., Zhang, X., Huang, J., Liu, D., Songyang, Z., 2015. The Daxx/Atrx Complex Protects Tandem Repetitive Elements during DNA Hypomethylation by Promoting H3K9 Trimethylation. Cell Stem Cell 17, 273–286. https://doi.org/10.1016/j.stem.2015.07.022

Hoelper, D., Huang, H., Jain, A.Y., Patel, D.J., Lewis, P.W., 2017. Structural and mechanistic insights into ATRX-dependent and -independent functions of the histone chaperone DAXX. Nat. Commun. 8, 1193. https://doi.org/10.1038/s41467-017-01206-y

Iwase, S., Xiang, B., Ghosh, S., Ren, T., Lewis, P.W., Cochrane, J.C., Allis, C.D., Picketts, D.J., Patel, D.J., Li, H., Shi, Y., 2011. ATRX ADD domain links an atypical histone methylation recognition mechanism to human mental-retardation syndrome. Nat. Struct. Mol. Biol. 18, 769–776. https://doi.org/10.1038/nsmb.2062

Jackson, J.P., Lindroth, A.M., Cao, X., Jacobsen, S.E., 2002. Control of CpNpG DNA methylation by the KRYPTONITE histone H3 methyltransferase. Nature 416, 556–560. https://doi.org/10.1038/nature731

Ji, J., Quindipan, C., Parham, D., Shen, L., Ruble, D., Bootwalla, M., Maglinte, D.T., Gai, X., Saitta, S.C., Biegel, J.A., Mascarenhas, L., 2017. Inherited germline *ATRX* mutation in two brothers with ATR-X syndrome and osteosarcoma. Am. J. Med. Genet. A. 173, 1390–1395. https://doi.org/10.1002/ajmg.a.38184

Jin, C., Zang, C., Wei, G., Cui, K., Peng, W., Zhao, K., Felsenfeld, G., 2009. H3.3/H2A.Z double variant-containing nucleosomes mark “nucleosome-free regions” of active promoters and other regulatory regions. Nat. Genet. 41, 941–945. https://doi.org/10.1038/ng.409

Jones, W.D., Dafou, D., McEntagart, M., Woollard, W.J., Elmslie, F.V., HolderEspinasse, M., Irving, M., Saggar, A.K., Smithson, S., Trembath, R.C., Deshpande, C., Simpson, M.A., 2012. De Novo Mutations in MLL Cause Wiedemann-Steiner Syndrome. Am. J. Hum. Genet. 91, 358–364. https://doi.org/10.1016/j.ajhg.2012.06.008

Kang, M.A., Lee, J.-S., 2021. A Newly Assigned Role of CTCF in Cellular Response to Broken DNAs. Biomolecules 11, 363. https://doi.org/10.3390/biom11030363

Kernohan, K.D., Jiang, Y., Tremblay, D.C., Bonvissuto, A.C., Eubanks, J.H., Mann, M.R.W., Bérubé, N.G., 2010a. ATRX Partners with Cohesin and MeCP2 and Contributes to Developmental Silencing of Imprinted Genes in the Brain. Dev. Cell 18, 191–202. https://doi.org/10.1016/j.devcel.2009.12.017

Kernohan, K.D., Jiang, Y., Tremblay, D.C., Bonvissuto, A.C., Eubanks, J.H., Mann, M.R.W., Bérubé, N.G., 2010b. ATRX partners with cohesin and MeCP2 and contributes to developmental silencing of imprinted genes in the brain. Dev. Cell 18, 191–202. https://doi.org/10.1016/j.devcel.2009.12.017

Kernohan, K.D., Vernimmen, D., Gloor, G.B., Bérubé, N.G., 2014. Analysis of neonatal brain lacking ATRX or MeCP2 reveals changes in nucleosome density, CTCF binding and chromatin looping. Nucleic Acids Res. 42, 8356–8368. https://doi.org/10.1093/nar/gku564

Killela, P.J., Reitman, Z.J., Jiao, Y., Bettegowda, C., Agrawal, N., Diaz, L.A., Friedman, A.H., Friedman, H., Gallia, G.L., Giovanella, B.C., Grollman, A.P., He, T.-C., He, Y., Hruban, R.H., Jallo, G.I., Mandahl, N., Meeker, A.K., Mertens, F., Netto, G.J., Rasheed, B.A., Riggins, G.J., Rosenquist, T.A., Schiffman, M., Shih, I.-M., Theodorescu, D., Torbenson, M.S., Velculescu, V.E., Wang, T.-L., Wentzensen, N., Wood, L.D., Zhang, M., McLendon, R.E., Bigner, D.D., Kinzler, K.W., Vogelstein, B., Papadopoulos, N., Yan, H., 2013. TERT promoter mutations occur frequently in gliomas and a subset of tumors derived from cells with low rates of self-renewal. Proc. Natl. Acad. Sci. U. S. A. 110, 6021–6026. https://doi.org/10.1073/pnas.1303607110

Kim, J., Sun, C., Tran, A.D., Chin, P.-J., Ruiz, P.D., Wang, K., Gibbons, R.J., Gamble, M.J., Liu, Y., Oberdoerffer, P., 2019. The macroH2A1.2 histone variant links ATRX loss to alternative telomere lengthening. Nat. Struct. Mol. Biol. 26, 213–219. https://doi.org/10.1038/s41594-019-0192-3

Kovatcheva, M., Liao, W., Klein, M.E., Robine, N., Geiger, H., Crago, A.M., Dickson, M.A., Tap, W.D., Singer, S., Koff, A., 2017. ATRX is a regulator of therapy induced senescence in human cells. Nat. Commun. 8, 386. https://doi.org/10.1038/s41467-017-00540-5

Kunarso, G., Chia, N.-Y., Jeyakani, J., Hwang, C., Lu, X., Chan, Y.-S., Ng, H.-H., Bourque, G., 2010. Transposable elements have rewired the core regulatory network of human embryonic stem cells. Nat. Genet. 42, 631–634. https://doi.org/10.1038/ng.600

Law, J.A., Jacobsen, S.E., 2010. Establishing, maintaining and modifying DNA methylation patterns in plants and animals. Nat. Rev. Genet. 11, 204–220. https://doi.org/10.1038/nrg2719

Law, M.J., Lower, K.M., Voon, H.P.J., Hughes, J.R., Garrick, D., Viprakasit, V., Mitson, M., De Gobbi, M., Marra, M., Morris, A., Abbott, A., Wilder, S.P., Taylor, S., Santos, G.M., Cross, J., Ayyub, H., Jones, S., Ragoussis, J., Rhodes, D., Dunham, I., Higgs, D.R., Gibbons, R.J., 2010. ATR-X syndrome protein targets tandem repeats and influences allele-specific expression in a size-dependent manner. Cell 143, 367–378. https://doi.org/10.1016/j.cell.2010.09.023

Lee, N.G., Hong, Y.K., Yu, S.Y., Han, S.Y., Geum, D., Cho, K.S., 2007. dXNP, a *Drosophila* homolog of XNP/ATRX, induces apoptosis via Jun-N-terminal kinase activation. FEBS Lett. 581, 2625–2632. https://doi.org/10.1016/j.febslet.2007.05.005

Leung, J.W.-C., Ghosal, G., Wang, W., Shen, X., Wang, J., Li, L., Chen, J., 2013. Alpha Thalassemia/Mental Retardation Syndrome X-linked Gene Product ATRX Is Required for Proper Replication Restart and Cellular Resistance to Replication Stress. J. Biol. Chem. 288, 6342–6350. https://doi.org/10.1074/jbc.M112.411603

Lewis, P.W., Elsaesser, S.J., Noh, K.-M., Stadler, S.C., Allis, C.D., 2010. Daxx is an H3.3-specific histone chaperone and cooperates with ATRX in replicationindependent chromatin assembly at telomeres. Proc. Natl. Acad. Sci. 107, 14075–14080. https://doi.org/10.1073/pnas.1008850107

Liang, J., Liu, H., Li, G., Qian, J., Gao, R., Zhou, Y., Wang, X., 2020a. Global changes in chromatin accessibility and transcription following *ATRX* inactivation in human cancer cells. FEBS Lett. 594, 67–78. https://doi.org/10.1002/1873-3468.13549

Liang, J., Liu, H., Li, G., Qian, J., Gao, R., Zhou, Y., Wang, X., 2020b. Global changes in chromatin accessibility and transcription following ATRX inactivation in human cancer cells. FEBS Lett. 594, 67–78. https://doi.org/10.1002/1873-3468.13549

Lovejoy, C.A., Li, W., Reisenweber, S., Thongthip, S., Bruno, J., De Lange, T., De, S., Petrini, J.H.J., Sung, P.A., Jasin, M., Rosenbluh, J., Zwang, Y., Weir, B.A., Hatton, C., Ivanova, E., Macconaill, L., Hanna, M., Hahn, W.C., Lue, N.F., Reddel, R.R., Jiao, Y., Kinzler, K., Vogelstein, B., Papadopoulos, N., Meeker, A.K., for the ALT Starr Cancer Consortium, 2012. Loss of ATRX, Genome Instability, and an Altered DNA Damage Response Are Hallmarks of the Alternative Lengthening of Telomeres Pathway. PLoS Genet. 8, e1002772.

https://doi.org/10.1371/journal.pgen.1002772
Lynskey, M.L., Brown, E.E., Bhargava, R., Wondisford, A.R., Ouriou, J.-B., Freund, O., Bowman, R.W., Smith, B.A., Lardo, S.M., Schamus-Hayes, S., Hainer, S.J., O'Sullivan, R.J., 2024. HIRA protects telomeres against R-loop-induced instability in ALT cancer cells. Cell Rep. 43, 114964. https://doi.org/10.1016/j.celrep.2024.114964
Mach, P., Kos, P.I., Zhan, Y., Cramard, J., Gaudin, S., Tünnermann, J., Marchi, E., Eglinger, J., Zuin, J., Kryzhanovska, M., Smallwood, S., Gelman, L., Roth, G., Nora, E.P., Tiana, G., Giorgetti, L., 2022a. Cohesin and CTCF control the dynamics of chromosome folding. Nat. Genet. 54, 1907–1918. https://doi.org/10.1038/s41588-022-01232-7
Mach, P., Kos, P.I., Zhan, Y., Cramard, J., Gaudin, S., Tünnermann, J., Marchi, E., Eglinger, J., Zuin, J., Kryzhanovska, M., Smallwood, S., Gelman, L., Roth, G., Nora, E.P., Tiana, G., Giorgetti, L., 2022b. Cohesin and CTCF control the dynamics of chromosome folding. Nat. Genet. 54, 1907–1918. https://doi.org/10.1038/s41588-022-01232-7
Marano, D., Fioriniello, S., Fiorillo, F., Gibbons, R.J., D'Esposito, M., Della Ragione, F., 2019. ATRX Contributes to MeCP2-Mediated Pericentric Heterochromatin Organization during Neural Differentiation. Int. J. Mol. Sci. 20, 5371. https://doi.org/10.3390/ijms20215371
Marchal, C., Sasaki, T., Vera, D., Wilson, K., Sima, J., Rivera-Mulia, J.C., TrevillaGarcía, C., Nogues, C., Nafie, E., Gilbert, D.M., 2018. Genome-wide analysis of replication timing by next-generation sequencing with E/L Repli-seq. Nat. Protoc. 13, 819–839. https://doi.org/10.1038/nprot.2017.148
Matsui, T., Leung, D., Miyashita, H., Maksakova, I.A., Miyachi, H., Kimura, H., Tachibana, M., Lorincz, M.C., Shinkai, Y., 2010. Proviral silencing in embryonic stem cells requires the histone methyltransferase ESET. Nature 464, 927–931. https://doi.org/10.1038/nature08858
Monteagudo-Sánchez, A., Richard Albert, J., Scarpa, M., Noordermeer, D., Greenberg, M.V.C., 2024. The impact of the embryonic DNA methylation program on CTCFmediated genome regulation. Nucleic Acids Res. 52, 10934–10950. https://doi.org/10.1093/nar/gkae724
Mossink, B., Negwer, M., Schubert, D., Nadif Kasri, N., 2021. The emerging role of chromatin remodelers in neurodevelopmental disorders: a developmental perspective. Cell. Mol. Life Sci. 78, 2517–2563. https://doi.org/10.1007/s00018020-03714-5
Nan, X., Hou, J., Maclean, A., Nasir, J., Lafuente, M.J., Shu, X., Kriaucionis, S., Bird, A., 2007. Interaction between chromatin proteins MECP2 and ATRX is disrupted by mutations that cause inherited mental retardation. Proc. Natl. Acad. Sci. 104, 2709–2714. https://doi.org/10.1073/pnas.0608056104
Neale, B.M., Kou, Y., Liu, L., Ma'ayan, A., Samocha, K.E., Sabo, A., Lin, C.-F., Stevens, C., Wang, L.-S., Makarov, V., Polak, P., Yoon, S., Maguire, J., Crawford, E.L., Campbell, N.G., Geller, E.T., Valladares, O., Schafer, C., Liu, H., Zhao, T., Cai,

G., Lihm, J., Dannenfelser, R., Jabado, O., Peralta, Z., Nagaswamy, U., Muzny, D., Reid, J.G., Newsham, I., Wu, Y., Lewis, L., Han, Y., Voight, B.F., Lim, E., Rossin, E., Kirby, A., Flannick, J., Fromer, M., Shakir, K., Fennell, T., Garimella, K., Banks, E., Poplin, R., Gabriel, S., DePristo, M., Wimbish, J.R., Boone, B.E., Levy, S.E., Betancur, C., Sunyaev, S., Boerwinkle, E., Buxbaum, J.D., Cook Jr, E.H., Devlin, B., Gibbs, R.A., Roeder, K., Schellenberg, G.D., Sutcliffe, J.S., Daly, M.J., 2012. Patterns and rates of exonic de novo mutations in autism spectrum disorders. Nature 485, 242–245. https://doi.org/10.1038/nature11011

Noh, K.-M., Maze, I., Zhao, D., Xiang, B., Wenderski, W., Lewis, P.W., Shen, L., Li, H., Allis, C.D., 2015. ATRX tolerates activity-dependent histone H3 methyl/phos switching to maintain repetitive element silencing in neurons. Proc. Natl. Acad. Sci. U. S. A. 112, 6820–6827. https://doi.org/10.1073/pnas.1411258112

Nora, E.P., Caccianini, L., Fudenberg, G., So, K., Kameswaran, V., Nagle, A., Uebersohn, A., Hajj, B., Saux, A.L., Coulon, A., Mirny, L.A., Pollard, K.S., Dahan, M., Bruneau, B.G., 2020. Molecular basis of CTCF binding polarity in genome folding. Nat. Commun. 11, 5612. https://doi.org/10.1038/s41467-020-19283-x

Nora, E.P., Goloborodko, A., Valton, A.-L., Gibcus, J.H., Uebersohn, A., Abdennur, N., Dekker, J., Mirny, L.A., Bruneau, B.G., 2017. Targeted Degradation of CTCF Decouples Local Insulation of Chromosome Domains from Genomic Compartmentalization. Cell 169, 930-944.e22. https://doi.org/10.1016/j.cell.2017.05.004

Park, J., Lee, H., Han, N., Kwak, S., Lee, H.-T., Kim, J.-H., Kang, K., Youn, B.H., Yang, J.-H., Jeong, H.-J., Kang, J.-S., Kim, S.-Y., Han, J.-W., Youn, H.-D., Cho, E.-J., 2018. Long non-coding RNA ChRO1 facilitates ATRX/DAXX-dependent H3.3 deposition for transcription-associated heterochromatin reorganization. Nucleic Acids Res. 46, 11759–11775. https://doi.org/10.1093/nar/gky923

Pinto, D., Delaby, E., Merico, D., Barbosa, M., Merikangas, A., Klei, L., Thiruvahindrapuram, B., Xu, X., Ziman, R., Wang, Z., Vorstman, J.A.S., Thompson, A., Regan, R., Pilorge, M., Pellecchia, G., Pagnamenta, A.T., Oliveira, B., Marshall, C.R., Magalhaes, T.R., Lowe, J.K., Howe, J.L., Griswold, A.J., Gilbert, J., Duketis, E., Dombroski, B.A., De Jonge, M.V., Cuccaro, M., Crawford, E.L., Correia, C.T., Conroy, J., Conceição, I.C., Chiocchetti, A.G., Casey, J.P., Cai, G., Cabrol, C., Bolshakova, N., Bacchelli, E., Anney, R., Gallinger, S., Cotterchio, M., Casey, G., Zwaigenbaum, L., Wittemeyer, K., Wing, K., Wallace, S., van Engeland, H., Tryfon, A., Thomson, S., Soorya, L., Rogé, B., Roberts, W., Poustka, F., Mouga, S., Minshew, N., McInnes, L.A., McGrew, S.G., Lord, C., Leboyer, M., Le Couteur, A.S., Kolevzon, A., Jiménez González, P., Jacob, S., Holt, R., Guter, S., Green, J., Green, A., Gillberg, C., Fernandez, B.A., Duque, F., Delorme, R., Dawson, G., Chaste, P., Café, C., Brennan, S., Bourgeron, T., Bolton, P.F., Bölte, S., Bernier, R., Baird, G., Bailey, A.J., Anagnostou, E., Almeida, J., Wijsman, E.M., Vieland, V.J., Vicente, A.M., Schellenberg, G.D., Pericak-Vance, M., Paterson, A.D., Parr, J.R., Oliveira, G., Nurnberger, J.I., Monaco, A.P., Maestrini, E., Klauck, S.M., Hakonarson, H., Haines, J.L.,

Geschwind, D.H., Freitag, C.M., Folstein, S.E., Ennis, S., Coon, H., Battaglia, A., Szatmari, P., Sutcliffe, J.S., Hallmayer, J., Gill, M., Cook, E.H., Buxbaum, J.D., Devlin, B., Gallagher, L., Betancur, C., Scherer, S.W., 2014. Convergence of Genes and Cellular Pathways Dysregulated in Autism Spectrum Disorders. Am. J. Hum. Genet. 94, 677–694. https://doi.org/10.1016/j.ajhg.2014.03.018

Raghunandan, M., Yeo, J.E., Walter, R., Saito, K., Harvey, A.J., Ittershagen, S., Lee, E.A., Yang, J., Hoatlin, M.E., Bielinsky, A.K., Hendrickson, E.A., Schärer, O., Sobeck, A., 2020. Functional cross talk between the Fanconi anemia and ATRX/DAXX histone chaperone pathways promotes replication fork recovery. Hum. Mol. Genet. 29, 1083–1095. https://doi.org/10.1093/hmg/ddz250

Raimer Young, H.M., Hou, P.-C., Bartosik, A.R., Atkin, N.D., Wang, L., Wang, Z., Ratan, A., Zang, C., Wang, Y.-H., 2024. DNA fragility at topologically associated domain boundaries is promoted by alternative DNA secondary structure and topoisomerase II activity. Nucleic Acids Res. 52, 3837–3855. https://doi.org/10.1093/nar/gkae164

Rao, S.S.P., Huntley, M.H., Durand, N.C., Stamenova, E.K., Bochkov, I.D., Robinson, J.T., Sanborn, A.L., Machol, I., Omer, A.D., Lander, E.S., Aiden, E.L., 2014. A 3D map of the human genome at kilobase resolution reveals principles of chromatin looping. Cell 159, 1665–1680. https://doi.org/10.1016/j.cell.2014.11.021

Ray-Gallet, D., Woolfe, A., Vassias, I., Pellentz, C., Lacoste, N., Puri, A., Schultz, D.C., Pchelintsev, N.A., Adams, P.D., Jansen, L.E.T., Almouzni, G., 2011. Dynamics of Histone H3 Deposition In Vivo Reveal a Nucleosome Gap-Filling Mechanism for H3.3 to Maintain Chromatin Integrity. Mol. Cell 44, 928–941. https://doi.org/10.1016/j.molcel.2011.12.006

Ren, W., Fan, H., Grimm, S.A., Guo, Y., Kim, J.J., Yin, J., Li, L., Petell, C.J., Tan, X.-F., Zhang, Z.-M., Coan, J.P., Gao, L., Cai, L., Detrick, B., Çetin, B., Cui, Q., Strahl, B.D., Gozani, O., Wang, Y., Miller, K.M., O'Leary, S.E., Wade, P.A., Patel, D.J., Wang, G.G., Song, J., 2020. Direct readout of heterochromatic H3K9me3 regulates DNMT1-mediated maintenance DNA methylation. Proc. Natl. Acad. Sci.
U. S. A. 117, 18439–18447. https://doi.org/10.1073/pnas.2009316117

Ryba, T., Hiratani, I., Lu, J., Itoh, M., Kulik, M., Zhang, J., Schulz, T.C., Robins, A.J., Dalton, S., Gilbert, D.M., 2010. Evolutionarily conserved replication timing profiles predict long-range chromatin interactions and distinguish closely related cell types. Genome Res. 20, 761–770. https://doi.org/10.1101/gr.099655.109

Sadic, D., Schmidt, K., Groh, S., Kondofersky, I., Ellwart, J., Fuchs, C., Theis, F.J., Schotta, G., 2015. Atrx promotes heterochromatin formation at retrotransposons. EMBO Rep. 16, 836–850. https://doi.org/10.15252/embr.201439937

Sarma, K., Cifuentes-Rojas, C., Ergun, A., del Rosario, A., Jeon, Y., White, F., Sadreyev, R., Lee, J.T., 2014. ATRX Directs Binding of PRC2 to Xist RNA and Polycomb Targets. Cell 159, 869–883. https://doi.org/10.1016/j.cell.2014.10.019

Shafiq, S., Ghahramani, A., Mansour, K., Pena-Ortiz, M., Sunstrum, J.K., Pavlovic, M., Jiang, Y., Rowland, M.E., Inoue, W., Bérubé, N.G., 2025. Microglial deficiency in

the ATRX chromatin remodeler elicits a viral mimicry immune response that impacts neuronal function and behavior. PLoS Biol. 23, e3002659. https://doi.org/10.1371/journal.pbio.3002659

Sima, J., Chakraborty, A., Dileep, V., Michalski, M., Klein, K.N., Holcomb, N.P., Turner, J.L., Paulsen, M.T., Rivera-Mulia, J.C., Trevilla-Garcia, C., Bartlett, D.A., Zhao, P.A., Washburn, B.K., Nora, E.P., Kraft, K., Mundlos, S., Bruneau, B.G., Ljungman, M., Fraser, P., Ay, F., Gilbert, D.M., 2019. Identifying cis Elements for Spatiotemporal Control of Mammalian DNA Replication. Cell 176, 816-830.e18. https://doi.org/10.1016/j.cell.2018.11.036

Spirito, G., Filosi, M., Domenici, E., Mangoni, D., Gustincich, S., Sanges, R., 2023. Exploratory analysis of L1 retrotransposons expression in autism. Mol. Autism 14, 22. https://doi.org/10.1186/s13229-023-00554-5

Tafessu, A., O'Hara, R., Martire, S., Dube, A.L., Saha, P., Gant, V.U., Banaszynski, L.A., 2023. H3.3 contributes to chromatin accessibility and transcription factor binding at promoter-proximal regulatory elements in embryonic stem cells. Genome Biol. 24, 25. https://doi.org/10.1186/s13059-023-02867-3

Tagami, H., Ray-Gallet, D., Almouzni, G., Nakatani, Y., 2004. Histone H3.1 and H3.3 Complexes Mediate Nucleosome Assembly Pathways Dependent or Independent of DNA Synthesis. Cell 116, 51–61. https://doi.org/10.1016/S00928674(03)01064-X

Tamaru, H., Selker, E.U., 2001. A histone H3 methyltransferase controls DNA methylation in Neurospora crassa. Nature 414, 277–283. https://doi.org/10.1038/35104508

Tamaru, H., Zhang, X., McMillen, D., Singh, P.B., Nakayama, J., Grewal, S.I., Allis, C.D., Cheng, X., Selker, E.U., 2003. Trimethylated lysine 9 of histone H3 is a mark for DNA methylation in Neurospora crassa. Nat. Genet. 34, 75–79. https://doi.org/10.1038/ng1143

Teng, Y.-C., Sundaresan, A., O'Hara, R., Gant, V.U., Li, M., Martire, S., Warshaw, J.N., Basu, A., Banaszynski, L.A., 2021. ATRX promotes heterochromatin formation to protect cells from G-quadruplex DNA-mediated stress. Nat. Commun. 12, 3887. https://doi.org/10.1038/s41467-021-24206-5

The DDD Study, Homozygosity Mapping Collaborative for Autism, UK10K Consortium, The Autism Sequencing Consortium, De Rubeis, S., He, X., Goldberg, A.P., Poultney, C.S., Samocha, K., Ercument Cicek, A., Kou, Y., Liu, L., Fromer, M., Walker, S., Singh, T., Klei, L., Kosmicki, J., Fu, S.-C., Aleksic, B., Biscaldi, M., Bolton, P.F., Brownfeld, J.M., Cai, J., Campbell, N.G., Carracedo, A., Chahrour, M.H., Chiocchetti, A.G., Coon, H., Crawford, E.L., Crooks, L., Curran, S.R., Dawson, G., Duketis, E., Fernandez, B.A., Gallagher, L., Geller, E., Guter, S.J., Sean Hill, R., Ionita-Laza, I., Jimenez Gonzalez, P., Kilpinen, H., Klauck, S.M., Kolevzon, A., Lee, I., Lei, J., Lehtimäki, T., Lin, C.-F., Ma'ayan, A., Marshall, C.R., McInnes, A.L., Neale, B., Owen, M.J., Ozaki, N., Parellada, M., Parr, J.R., Purcell, S., Puura, K., Rajagopalan, D., Rehnström, K., Reichenberg, A., Sabo, A., Sachse, M., Sanders, S.J., Schafer, C., Schulte-Rüther, M., Skuse, D.,

Stevens, C., Szatmari, P., Tammimies, K., Valladares, O., Voran, A., Wang, L.-S., Weiss, L.A., Jeremy Willsey, A., Yu, T.W., Yuen, R.K.C., Cook, E.H., Freitag, C.M., Gill, M., Hultman, C.M., Lehner, T., Palotie, A., Schellenberg, G.D., Sklar, P., State, M.W., Sutcliffe, J.S., Walsh, C.A., Scherer, S.W., Zwick, M.E., Barrett, J.C., Cutler, D.J., Roeder, K., Devlin, B., Daly, M.J., Buxbaum, J.D., 2014. Synaptic, transcriptional and chromatin genes disrupted in autism. Nature 515, 209–215. https://doi.org/10.1038/nature13772

Thompson, P.J., Macfarlan, T.S., Lorincz, M.C., 2016. Long Terminal Repeats: From Parasitic Elements to Building Blocks of the Transcriptional Regulatory Repertoire. Mol. Cell 62, 766–776. https://doi.org/10.1016/j.molcel.2016.03.029

Truch, J., Downes, D.J., Scott, C., Gür, E.R., Telenius, J.M., Repapi, E., Schwessinger, R., Gosden, M., Brown, J.M., Taylor, S., Cheong, P.L., Hughes, J.R., Higgs, D.R., Gibbons, R.J., 2022. The chromatin remodeller ATRX facilitates diverse nuclear processes, in a stochastic manner, in both heterochromatin and euchromatin. Nat. Commun. 13, 3485. https://doi.org/10.1038/s41467-022-31194-7

Tsai, R.-X., Fang, K.-C., Yang, P.-C., Hsieh, Y.-H., Chiang, I.-T., Chen, Y., Lee, H.-G., Lee, J.T., Chu, H.-P.C., 2022. TERRA regulates DNA G-quadruplex formation and ATRX recruitment to chromatin. Nucleic Acids Res. 50, 12217–12234. https://doi.org/10.1093/nar/gkac1114

Tyagi, M., Imam, N., Verma, K., Patel, A.K., 2016. Chromatin remodelers: We are the drivers!! Nucleus 7, 388–404. https://doi.org/10.1080/19491034.2016.1211217

Valenzuela, M., Amato, R., Sgura, A., Antoccia, A., Berardinelli, F., 2021. The Multiple Facets of ATRX Protein. Cancers 13, 2211. https://doi.org/10.3390/cancers13092211

Valle-García, D., Qadeer, Z.A., McHugh, D.S., Ghiraldini, F.G., Chowdhury, A.H., Hasson, D., Dyer, M.A., Recillas-Targa, F., Bernstein, E., 2016. ATRX binds to atypical chromatin domains at the 3’ exons of zinc finger genes to preserve H3K9me3 enrichment. Epigenetics 11, 398–414. https://doi.org/10.1080/15592294.2016.1169351

Voon, H.P.J., Hughes, J.R., Rode, C., De La Rosa-Velázquez, I.A., Jenuwein, T., Feil, R., Higgs, D.R., Gibbons, R.J., 2015. ATRX Plays a Key Role in Maintaining Silencing at Interstitial Heterochromatic Loci and Imprinted Genes. Cell Rep. 11, 405–418. https://doi.org/10.1016/j.celrep.2015.03.036

Voon, H.P.J., Wong, L.H., 2016. New players in heterochromatin silencing: histone variant H3.3 and the ATRX/DAXX chaperone. Nucleic Acids Res. 44, 1496–1501. https://doi.org/10.1093/nar/gkw012

Wada, T., Sugie, H., Fukushima, Y., Saitoh, S., 2005. Non-skewed X-inactivation may cause mental retardation in a female carrier of X-linked α-thalassemia/mental retardation syndrome (ATR-X): X-inactivation study of nine female carriers of ATR-X. Am. J. Med. Genet. A. 138A, 18–20. https://doi.org/10.1002/ajmg.a.30901

Wagner, V.F., Hillman, P.R., Britt, A.D., Ray, J.W., Farach, L.S., 2019. A De novo *HDAC2* variant in a patient with features consistent with Cornelia de Lange syndrome phenotype. Am. J. Med. Genet. A. 179, 852–856. https://doi.org/10.1002/ajmg.a.61101

Walsh, C.P., Chaillet, J.R., Bestor, T.H., 1998. Transcription of IAP endogenous retroviruses is constrained by cytosine methylation. Nat. Genet. 20, 116–117. https://doi.org/10.1038/2413

Wang, X., Zhao, Y., Zhang, J., Chen, Y., 2017. Structural basis for DAXX interaction with ATRX. Protein Cell 8, 767–771. https://doi.org/10.1007/s13238-017-0462-y

Wang, Y., Yang, J., Wild, A.T., Wu, W.H., Shah, R., Danussi, C., Riggins, G.J., Kannan, K., Sulman, E.P., Chan, T.A., Huse, J.T., 2019. G-quadruplex DNA drives genomic instability and represents a targetable molecular abnormality in ATRXdeficient malignant glioma. Nat. Commun. 10, 943. https://doi.org/10.1038/s41467-019-08905-8

Weth, O., Paprotka, C., Günther, K., Schulte, A., Baierl, M., Leers, J., Galjart, N., Renkawitz, R., 2014. CTCF induces histone variant incorporation, erases the H3K27me3 histone mark and opens chromatin. Nucleic Acids Res. 42, 11941–11951. https://doi.org/10.1093/nar/gku937

Wolf, G., Greenberg, D., Macfarlan, T.S., 2015. Spotting the enemy within: Targeted silencing of foreign DNA in mammalian genomes by the Krüppel-associated box zinc finger protein family. Mob. DNA 6, 17. https://doi.org/10.1186/s131000150050-8

Wong, E.W.P., Sahin, M., Yang, R., Lee, U., Li, D., Zhan, Y.A., Misra, R., Tomas, F., Alomran, N., Polyzos, A., Lee, C.J., Trieu, T., Martinez-Fundichely, A., Wiesner, T., Rosowicz, A., Cheng, S., Liu, C., Lallo, M., Shoushtari, A.N., Merghoub, T., Hamard, P.-J., Koche, R., Khurana, E., Apostolou, E., Zheng, D., Chen, Y., Leslie, C.S., Chi, P., 2025. Disruption of TAD hierarchy promotes LTR co-option in cancer. Nat. Genet. 57, 1754–1765. https://doi.org/10.1038/s41588-025-02239-6 Wong, L.H., McGhie, J.D., Sim, M., Anderson, M.A., Ahn, S., Hannan, R.D., George, A.J., Morgan, K.A., Mann, J.R., Choo, K.H.A., 2010. ATRX interacts with H3.3 in maintaining telomere structural integrity in pluripotent embryonic stem cells. Genome Res. 20, 351–360. https://doi.org/10.1101/gr.101477.109

Xie, M., Hong, C., Zhang, B., Lowdon, R.F., Xing, X., Li, D., Zhou, X., Lee, H.J., Maire, C.L., Ligon, K.L., Gascard, P., Sigaroudinia, M., Tlsty, T.D., Kadlecek, T., Weiss, A., O'Geen, H., Farnham, P.J., Madden, P.A.F., Mungall, A.J., Tam, A., Kamoh, B., Cho, S., Moore, R., Hirst, M., Marra, M.A., Costello, J.F., Wang, T., 2013. DNA hypomethylation within specific transposable element families associates with tissue-specific enhancer landscape. Nat. Genet. 45, 836–841. https://doi.org/10.1038/ng.2649

Xu, Q., Liu, Y., Wang, X., Tan, G., Li, H., Hulbert, S.W., Li, C., Hu, C., Xiong, Z., Xu, X., Jiang, Y., 2018. Autism-associated CHD8 deficiency impairs axon development and migration of cortical neurons. Mol. Autism 9, 65. https://doi.org/10.1186/s13229-018-0244-2

Yang, B.X., El Farran, C.A., Guo, H.C., Yu, T., Fang, H.T., Wang, H.F., Schlesinger, S., Seah, Y.F.S., Goh, G.Y.L., Neo, S.P., Li, Y., Lorincz, M.C., Tergaonkar, V., Lim, T.-M., Chen, L., Gunaratne, J., Collins, J.J., Goff, S.P., Daley, G.Q., Li, H., Bard, F.A., Loh, Y.-H., 2015. Systematic identification of factors for provirus silencing in embryonic stem cells. Cell 163, 230–245. https://doi.org/10.1016/j.cell.2015.08.037

Yang, J., Horton, J.R., Liu, B., Corces, V.G., Blumenthal, R.M., Zhang, X., Cheng, X., 2023. Structures of CTCF-DNA complexes including all 11 zinc fingers. Nucleic Acids Res. 51, 8447–8462. https://doi.org/10.1093/nar/gkad594

Yang, Y., Zhang, L., Xiong, C., Chen, J., Wang, L., Wen, Z., Yu, J., Chen, P., Xu, Y., Jin, J., Cai, Y., Li, G., 2022. HIRA complex presets transcriptional potential through coordinating depositions of the histone variants H3.3 and H2A.Z on the poised genes in mESCs. Nucleic Acids Res. 50, 191–206. https://doi.org/10.1093/nar/gkab1221

Zagirova, D., Kononkova, A., Vaulin, N., Khrameeva, E., 2024. From compartments to loops: understanding the unique chromatin organization in neuronal cells. Epigenetics Chromatin 17, 18. https://doi.org/10.1186/s13072-024-00538-6

Zhang, J., Hu, G., Lu, Y., Ren, H., Huang, Y., Wen, Y., Ji, B., Wang, D., Wang, Haidong, Liu, H., Ma, N., Zhang, L., Pan, G., Qu, Y., Wang, Hua, Zhang, W., Miao, Z., Yao, H., 2024. CTCF mutation at R567 causes developmental disorders via 3D genome rearrangement and abnormal neurodevelopment. Nat. Commun. 15, 5524. https://doi.org/10.1038/s41467-024-49684-1